12-1-2010

Abrupt Longitudinal Magnetic Field Changes in Flaring Active Regions

G. J.D. Petrie
National Solar Observatory

Jeffrey J. Sudol
West Chester University of Pennsylvania, jsudol@wcupa.edu

Recommended Citation
Petrie, G. J., & Sudol, J. J. (2010). Abrupt Longitudinal Magnetic Field Changes in Flaring Active Regions. *The Astrophysical Journal, 724*, 1218-1237. http://dx.doi.org/10.1088/0004-637X/724/2/1218

The Astrophysical Journal, 724:1218–1237, 2010 December 1 doi:10.1088/0004-637X/724/2/1218

ABRUPT LONGITUDINAL MAGNETIC FIELD CHANGES IN FLARING ACTIVE REGIONS

G. J. D. Petrie[1] and J. J. Sudol[2]
[1] National Solar Observatory, 950 N. Cherry Avenue, Tucson, AZ 85719, USA
[2] West Chester University, West Chester, PA 19383, USA
Received 2010 March 15; accepted 2010 September 23; published 2010 November 11

ABSTRACT

We characterize the changes in the longitudinal photospheric magnetic field during 38 X-class and 39 M-class flares within 65° of disk center using 1 minute GONG magnetograms. In all 77 cases, we identify at least one site in the flaring active region where clear, permanent, stepwise field changes occurred. The median duration of the field changes was about 15 minutes and was approximately equal for X-class and for M-class flares. The absolute values of the field changes ranged from the detection limit of ∼10 G to as high as ∼450 G in two exceptional cases. The median value was 69 G. Field changes were significantly stronger for X-class than for M-class flares and for limb flares than for disk-center flares. Longitudinal field changes less than 100 G tended to decrease longitudinal field strengths, both close to disk center and close to the limb, while field changes greater than 100 G showed no such pattern. Likewise, longitudinal flux strengths tended to decrease during flares. Flux changes, particularly net flux changes near disk center, correlated better than local field changes with *GOES* peak X-ray flux. The strongest longitudinal field and flux changes occurred in flares observed close to the limb. We estimate the change of Lorentz force associated with each flare and find that this is large enough in some cases to power seismic waves. We find that longitudinal field decreases would likely outnumber increases at all parts of the solar disk within 65° of disk center, as in our observations, if photospheric field tilts increase during flares as predicted by Hudson et al.

Key words: magnetic fields – Sun: flares – Sun: photosphere

1. INTRODUCTION

Solar flares are generally believed to be caused by strong, stressed, topologically complicated magnetic fields. The energy estimated to power a solar flare can only come from the magnetic field and this field must be sufficiently stressed to contain enough free energy to power the flare. The topology must be complicated enough to contain a magnetic null point for abrupt energy release to be possible (e.g., Priest & Forbes 2000; Aschwanden 2004). Magnetic gradient maps derived from GONG longitudinal magnetograms (Gallagher et al. 2002), now available at http://www.solarmonitor.org, are a useful diagnostic of flare activity (see also Brockman 2010). Photospheric field gradients have long been known to be related to flare activity in active regions (e.g., Zhang et al. 1994). For a long time, however, observational studies of flare-related changes in longitudinal (i.e., the component along the observer's line of sight) and vector photospheric magnetic fields were inconclusive because of limitations of instrument sensitivity, spatial resolution, cadence, and coverage (Rust 1974; Sakurai & Hiei 1996). Moreover, some apparent magnetic field changes associated with large flares were later found not to represent real magnetic field changes but were due to flare-induced changes in the spectral line profiles used in measuring magnetic field strength (Patterson 1984; Harvey 1986; Qiu & Gary 2003; Edelman et al. 2004). In the past 15 years or so, however, high-cadence measurements of the photospheric magnetic field have become sensitive enough to resolve fast and permanent field changes in the vicinity of and coincident with large solar flares.

Wang et al. (1992, 1994) found rapid and permanent field changes in flaring active regions, but a number of later studies produced inconclusive results; see the discussion in Wang (2006). Kosovichev & Zharkova (1999) reported a sudden decrease in magnetic energy near an X-class flare, during its impulsive phase. A short time later, Kosovichev & Zharkova (2001) reported on regions of permanent decrease of longitudinal magnetic flux in the vicinity of the magnetic neutral line near the 2001 July 14 "Bastille Day" flare and linked the change in flux to the release of magnetic energy. The Big Bear Solar Observatory (BBSO) group has also described numerous cases featuring the sudden appearance and persistence of unbalanced magnetic flux at the time of a flare (Spirock et al. 2002; Wang et al. 2002, 2004; Yurchyshyn et al. 2004). Using 1 minute GONG magnetograms, Sudol & Harvey (2005, henceforth referred to as SH05) characterized the spatial distribution, strength and rate of change of permanent field changes associated with 15 X-class flares. Field changes ranged from 30 G to almost 300 G with a median value of 90 G. They found that the majority of field changes occurred in regions where the field strength reached hundreds of gauss which suggests locations close to or within sunspots given the resolution of the data. Liu et al. (2005) studied one M-class and six X-class flares and reported a roughly even split of increasing and decreasing longitudinal magnetic flux in regions of penumbral decay.

Wang (2006) studied five flaring δ-spots using high-cadence Michelson Doppler Imager (MDI) longitudinal magnetograms and found clear changes in the magnetic gradient along the neutral lines in all cases: the gradient increased in three cases and decreased in two. The centers of mass of the two magnetic polarities converged/diverged in the cases with gradient increase/decrease. For 11 data sets where vector data were available, Wang & Liu (2010) found that the transverse field at the polarity inversion line invariably increased. For all but one of 18 cases where 1 minute longitudinal data were available, the limbward flux was observed to increase and the diskward flux to decrease.

The BBSO group has also found a consistent pattern of behavior in sunspot structure. Parts of the outer penumbral structures decay rapidly after many flares, while neighboring umbral cores and inner penumbal regions become darker (Wang et al. 2004, 2005, 2009; Deng et al. 2005; Liu et al. 2005). Meanwhile, transverse fields were found to decrease in the

regions of penumbral decay and to increase at the flare neutral lines. Wang et al. (2002) describe one extreme case in which the onset of an M-class flare coincided with the disappearance of a small sunspot. Li et al. (2009) found that during the 2006 December 13 X3.4 flare the mean inclination angle of the magnetic field increased in the part of the penumbra that decayed, whereas the inclination angle decreased in the part of the penumbra that was enhanced during the flare and near the magnetic neutral line.

In contrast, many theoretical models of flares have incorporated the assumption that photospheric fields should not change significantly during flares (e.g., Priest & Forbes 2002) and this trend continues to the present. Indeed, Mei & Lin (2008) attribute the observed field changes to the fact that the spectral lines used in the observations are not formed in the photosphere. However, the Ni I line at 676.8 nm used by GONG and MDI corresponds to a height of about 200 km above the solar surface, in the lower photosphere, where the physics is expected to be dominated by the fluid and not the magnetic field (e.g., Priest 1982). Fletcher & Hudson (2008) argue that large-scale Alfvén wave pulses transport energy and magnetic field changes from the flare site rapidly through the corona to the lower atmosphere. Related theoretical work (Hudson 2000; Hudson et al. 2008) predicts that the flaring magnetic fields undergo an implosion or inward contraction and become more horizontal as a result of flares.

In this paper, we extend the work of SH05 from a sample of 15 X-class flares that occurred over a period of two years to a total of 77 flares—38 X-class flares and 39 M-class flares down to M5.0—that occurred over a period of six years. As in SH05, we characterize the abrupt, longitudinal magnetic field changes associated with the flares at representative points in each active region. We report on the strength and duration of the field changes and the time of the field changes with respect to the *GOES* X-ray signatures of the flares. We also test for correlations between the field changes and background field strength, *GOES* X-ray flux, and position on the solar disk. We report separate statistics for subsets of the data set, partitioning the data according to *GOES* peak X-ray flux (X-class/M-class), strength of the field change (greater than/less than 100 G), and position on the solar disk (near disk center/near limb).

Whereas SH05 limited their study to field changes at representative points in each active region, we go one step further and calculate the change in the longitudinal magnetic flux over the entire active region and characterize these changes in a manner similar to the field changes. The magnetic flux may be a much more meaningful physical quantity for many purposes than the change in the field strength at any one location but more complicated because of the noise inherent in the data.

SH05 stated the expectation that the flux changes might correlate with *GOES* peak X-ray flux but did not test this correlation. We do so here, testing the correlation between both the field and flux changes and the *GOES* peak X-ray flux. Any significant correlation would suggest that the energetics of the X-ray emission and the energetics of the field/flux changes are related.

SH05 reported no significant correlation between field change and position on the solar disk. We check this result with our larger data set. Because we measure the longitudinal component of the photospheric field, whose tilt angle with respect to the surface varies as a simple function of position on the disk, any correlation between the field/flux changes and position on the disk tells us which component of the magnetic field tends to change most during the flare, assuming that the field changes in direction and not in magnitude.

Finally, we estimate the Lorentz forces associated with the field/flux changes using A. N. McClymont's incisive method (Anwar et al. 1993; Hudson et al. 2008). Based on estimates of the total magnetic flux change during a typical X-class flare, Hudson et al. (2008) estimated that changes in the photospheric field due to such flares might be energetically important for seismic waves. Here, we calculate forces corresponding to our measured field changes to see how energetically important changes in the photospheric field are in general.

The paper is organized as follows. The data are described in Section 2 and the analysis techniques in Section 3. The field and flux changes of the 77 flares are characterized in Sections 4 and 5. Correlation of field and flux changes with *GOES* peak X-ray flux is investigated in Section 6, and the dependence of field and flux changes on position on the solar disk is explored in Section 7. Estimates of the changes in Lorentz force during the flares are derived in Section 8. We discuss the implications of our work in Section 9 and conclude in Section 10.

2. THE DATA

Changes in the magnetic field during a solar flare occur on a timescale of 10 minutes. Photospheric line profile changes occur over a few minutes, and non-flaring active-region fields can evolve at a rate of a few gauss per minute (SH05). Hence, we need of order an hour of uninterrupted high-sensitivity, high-cadence data to distinguish field changes associated with a flare from other changes in the field.

Full-disk images of the relative Doppler shift of the Ni I line at 676.8 nm are available from each of the six GONG telescopes at a cadence of 1 minute, weather permitting. GONG's six stations together provide round-the-clock coverage with approximately an 87% duty cycle. The spatial sampling of the GONG images is $2\farcs5$ pixel^{-1} and the instrumental sensitivity is about 3 G pixel^{-1}. The GONG magnetograms therefore provide the magnetic sensitivity, high cadence, spatial resolution, and spatial and temporal coverage required for the study of magnetic field changes during flares. The magnetograms are derived from the difference between 1 second interleaved observations in right- and left-polarized light and their pixel values are given in meters per second. These are scaled to gauss using the factor 0.352 G m^{-1} s^{-1}.

We have analyzed 83 sets of GONG magnetograms for 38 X-class flares, including the 15 examined by SH05, and 39 M-class flares. Six flares were observed by two sites simultaneously. Between 2001 April and October, the instruments at the six GONG sites were upgraded to the current spatial scale of $2\farcs5$ pixel^{-1} and full-time magnetic measurements began. Of the hundreds of M- and X-class flares between them and the last major flares of Solar Cycle 23, we limited our attention to the most energetic flares with the best data coverage. In particular, we eliminated all flares weaker than M5.0 and all flares with an apparent central meridian longitude difference greater than 65° ($\mu \approx 0.42$). We further limited our attention to those flares for which GONG magnetograms are available of order 1 hr before and after the flare. The flares studied are identified in Tables 1 (M-class) and 2 (X-class).

Figure 1 shows the locations of the flares on the solar disk. These locations are derived from the *GOES* X-ray flare catalog and they are also listed in Tables 1 and 2. They are fairly evenly

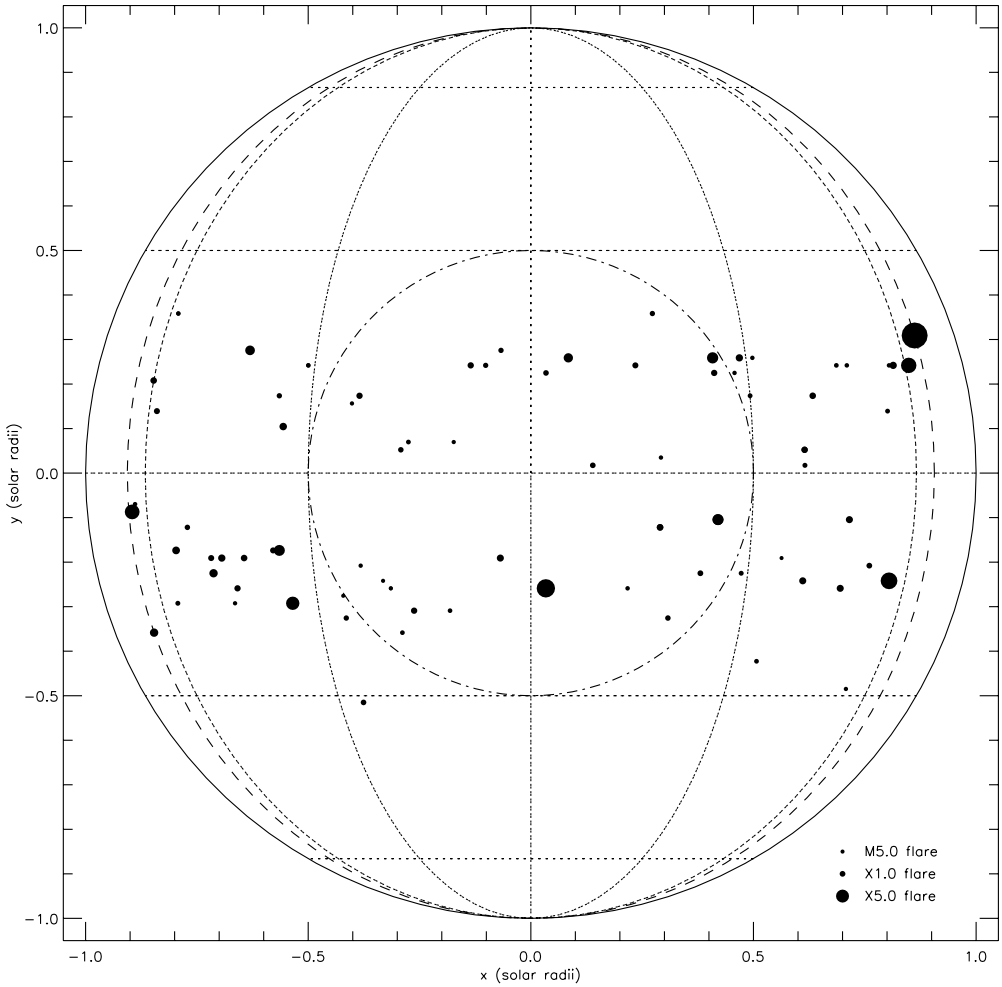

Figure 1. Positions of the 77 flares on the solar disk. The *GOES* peak X-ray flux is represented by circle size. The short-dashed lines mark 0°, ±30°, and ±60° longitude and latitude. Only flares located within 65° of central meridian, within the long-dashed lines, are studied. The dot-dashed circle $r = r_s/2$ separates locations deemed in this study to be near disk center ($r \leqslant r_s/2$) and those near the limb ($r > r_s/2$), where r_s is the solar disk radius in the image plane.

spread across the active belt of the Sun, between about ±30° of latitude.

3. DATA ANALYSIS

We remapped the active region associated with each flare as in SH05. We remapped each full-disk image to local heliographic coordinates on the plane tangent to a point near the center of the flaring active region using fourth-order spline interpolation. The remapped images are 256 × 256 pixels in size and represent and field of view of 32° × 32° in heliographic coordinates. We registered every remapped magnetogram to a reference image formed from the average of the 10 remapped magnetograms immediately preceding the flare. A full-disk image for the 2006 December 6 X6.5 flare is shown in Figure 2. This example is close to the 65° limit that we impose on the data. The registration reference image for the 2006 December 6 X6.5 flare is shown in Figure 3. To first order, the registration corrects for any drift of the active region with respect to the heliographic center of the frame and for any residual error in the orientation of solar north in the images. These shifts are executed as in SH05 by minimizing the difference between the square root of the absolute value of each frame and that of the reference image.

From each time series of remapped images, we constructed a time series of the field strength of each pixel for up to 4 hr, 2 hr before and after the start of the flare. As in SH05, we fit the function

$$B_l(t) = B_{\rm lin}(t) + B_{\rm step}(t), \tag{1}$$

where $B_{\rm lin}(t) = a + bt$ and

$$B_{\rm step}(t) = c\left\{1 + \frac{2}{\pi}\tan^{-1}\left[n(t - t_0)\right]\right\}, \tag{2}$$

to each time series. Here, t represents time, a and b model the background field evolution, c represents the half-amplitude of the field change, t_0 represents the midpoint of the field change, and n is the inverse of the timescale over which the field change occurs. The rate of field change is

$$\left.\frac{dB_{\rm step}}{dt}\right|_{t=t_0} = \frac{2cn}{\pi}, \tag{3}$$

where the field change and the duration of the change are given by $dB_l = 2c$ and $dt = \pi/n$, respectively. Like SH05, we simply characterize the field changes in this way without providing a physical model.

From the fits of the function $B_l(t)$ in Equation (1) to the time series for the pixels, we follow SH05 in creating spatial maps for each parameter in Equation (1). An example set of parameter maps for the 2006 December 6 flare is shown in Figure 4. Not all pixels are ultimately included in these maps.

Table 1
M-class Flares Studied in This Survey

Date (UT)	*GOES* Start Time	*GOES* Class	Location	NOAA Number
2001 Jun 22	2214	M6.2	N14W47	9503
2001 Jun 23	0010	M5.6	N09E24	9511
2001 Sep 5	1425	M6.0	N15W31	9601
2001 Sep 9	2040	M9.5	S31E26	9608
2001 Sep 16	0339	M5.6	S29W54	9608
2001 Oct 22	1427	M6.7	S21E18	9672
2001 Oct 23	0211	M6.5	S18E11	9672
2001 Nov 7	1930	M5.7	S17E44	9690
2001 Nov 8	0659	M9.1	S19W19	9687
2001 Nov 28	1626	M6.9	N04E16	9715
2001 Nov 29	1012	M5.5	N04E10	9715
2001 Dec 26	0432	M7.1	N08W54	9742
2002 Jan 9	1742	M9.5	N13W02	9773
2002 Mar 14	0138	M5.7	S12E23	9866
2002 Jul 11	1444	M5.8	N21E58	10030
2002 Jul 17	0658	M8.5	N21W17	10030
2002 Jul 26	2051	M8.7	S19E26	10044
2002 Aug 16	1132	M5.2	S14E20	10069
2002 Aug 20	0133	M5.0	S11W35	10069
2002 Oct 5	2042	M5.9	N14E31	10139
2002 Nov 18	0201	M7.4	S17E56	10198
2002 Dec 20	1313	M6.8	S25W34	10226
2003 Oct 26	2134	M7.6	N01W38	10484
2003 Oct 27	0921	M5.0	S16E26	10486
2003 Nov 20	0735	M9.6	N01W08	10501
2003 Nov 20	2342	M5.8	N02W17	10501
2004 Jan 17	1735	M5.0	S15E19	10540
2004 Jan 20	0729	M6.1	S15W13	10540
2004 Jul 13	0009	M6.7	N14W45	10646
2004 Jul 13	1924	M6.2	N14W56	10646
2004 Jul 20	1222	M8.6	N10E35	10652
2004 Jul 22	0014	M9.1	N03E17	10652
2004 Jul 25	0539	M7.1	N10W30	10652
2004 Aug 14	0536	M7.4	S13W29	10656
2004 Oct 10	1618	M5.9	N13W28	10656
2005 Jan 15	0426	M8.4	N14E06	10720
2005 Jan 15	0554	M8.6	N16E04	10720
2006 Dec 6	0802	M6.0	S04E63	10930
2007 Jun 4	0506	M8.9	S07E51	10960

Table 2
X-class Flares Studied in This Survey

Date (UT)	*GOES* Start Time	*GOES* Class	Location	NOAA Number
2001 Apr 2[a]	2132	X20.0	N18W65	9393
2001 Jun 23[a]	0402	X1.2	N10E23	9511
2001 Aug 25[a]	1623	X5.3	S17E34	9591
2001 Oct 19[a]	1613	X1.6	S17E34	9661
2001 Oct 22[a]	1744	X1.2	S18E16	9672
2001 Dec 11[a]	0758	X2.8	N16E41	9733
2002 May 20[a]	1521	X2.1	S21E65	9961
2002 Aug 21[a]	0528	X1.0	S12W51	10069
2003 Mar 17	1850	X1.5	S14W39	10314
2003 Mar 18	1151	X1.5	S15W46	10314
2003 May 27[a]	2256	X1.3	S07W17	10365
2003 May 28[a]	0017	X3.6	S06W25	10365
2003 Jun 10[a]	2319	X1.3	N10W40	10375
2003 Jun 11[a]	2001	X1.6	N14W57	10375
2003 Oct 19	1629	X1.1	N08E58	10484
2003 Oct 26[a]	0557	X1.2	S15E43	10486
2003 Oct 26	1721	X1.2	N02W38	10484
2003 Oct 29[a]	2037	X10.0	S15W02	10486
2003 Nov 2[a]	1703	X8.3	S14W56	10486
2004 Feb 26	0150	X1.1	N14W14	10564
2004 Jul 15	0130	X1.8	S10E34	10649
2004 Jul 15	1815	X1.6	S11E45	10649
2004 Jul 16	0143	X1.3	S11E41	10649
2004 Jul 16	1032	X1.1	S10E36	10649
2004 Jul 16	1349	X3.6	S10E35	10649
2004 Aug 13	1807	X1.0	S13W23	10656
2004 Oct 30	1138	X1.2	N13W25	10691
2005 Jan 1	0001	X1.7	N06E34	10715
2005 Jan 15	0022	X1.2	N14E08	10720
2005 Jan 15	2225	X2.6	N15W05	10720
2005 Jan 17	0659	X3.8	N15W25	10720
2005 Jan 20	0636	X7.1	N14W61	10720
2005 Jul 30	0617	X1.3	N12E60	10792
2005 Sep 10	1634	X1.1	S11E47	10808
2005 Sep 10	2130	X2.1	S13E47	10808
2005 Sep 13	1919	X1.5	S05E15	10808
2006 Dec 6	1829	X6.5	S05E64	10930
2006 Dec 14	2107	X1.5	S06W46	10930

Note. [a] Flares studied by SH05.

To avoid spurious fits of Equation (1) to flare-emission transients or to noise spikes, we include in these maps only those pixels exhibiting reasonably sized field changes ($|2c| < 500$ G) with steps of reasonably short duration ($\pi n^{-1} \leqslant 40$ minutes) and with the time of the step occurring within 20 minutes of the *GOES* flare start time. In the example in Figure 4, the a and c maps are almost inverses of each other showing in this particular case that most of the field changes reduce the field strength (see also SH05's Figure 2). The neutral lines of the two maps do not coincide, however, as there is a small region of increasing longitudinal field at the southern tip of the region of negative polarity. The field changes vary widely in duration and some variation in start times is evident in the n^{-1} and t_0 maps, respectively. Some field changes that occur early in the largest region of positive polarity close to the neutral line appear to propagate southwest across this region. This phenomenon is similar to that observed in the 2001 December 11 flare by SH05. The σ^2 map shows the scatter in the data with respect to the fit of Equation (1) to the data. The scatter (the noise) is greatest where the field is strongest and the field gradient is steepest. Therefore, the σ^2 map tends to resemble the absolute value of the a map. This is the case in our example in Figure 4 except that the strong positive region in the southwest of the active region does not appear strongly in the σ^2 map because the noise level in the southwest is unusually low.

The GONG instrumentation is identical in design across the network so that images taken simultaneously by two different telescopes should be nearly identical. We compared pairs of parameter maps for each of the six flares observed by two sites simultaneously. While instrumental differences and differences in seeing conditions inevitably prevent perfect matches between the image pairs, the close resemblance between each pair provides a foundation for confidence in our results. SH05 already verified that the analysis gave very similar results when applied to GONG and MDI data for the 2003 October 29 flare.

The remapped images for a given flare are stacked to form a space-time data cube. Figure 5 shows the evolution of a 16×16 subset of pixels in the form of a 16×16 mosaic of plots of field strength against time arranged to reflect the spatial distribution of the pixels. In each individual plot of the mosaic, the horizontal axis is time, spanning the 4 hr duration of the time series centered at the *GOES* start time of the flare, and the vertical axis is field intensity. The region chosen for this particular mosaic straddles the neutral line of the field-change map (parameter

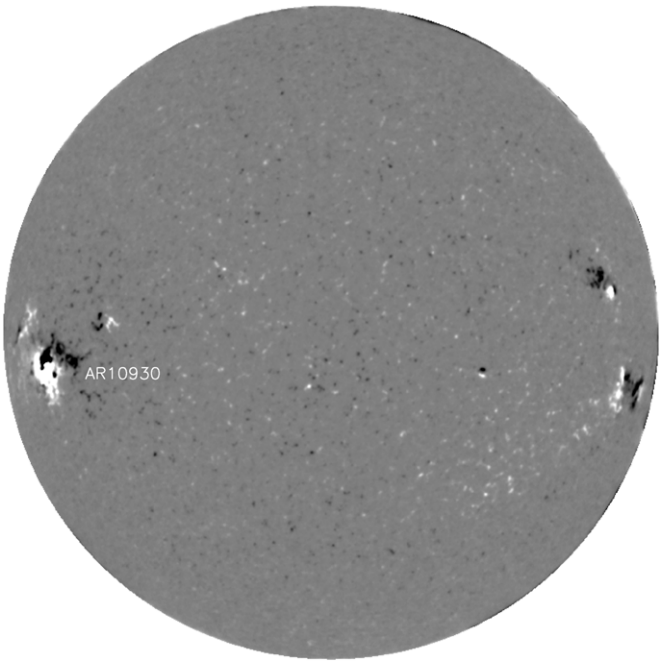

Figure 2. Average of the ten 1 minute GONG longitudinal full-disk magnetograms immediately before the X6.5 flare observed on 2006 December 6 at 1829 UT in active region 10930.

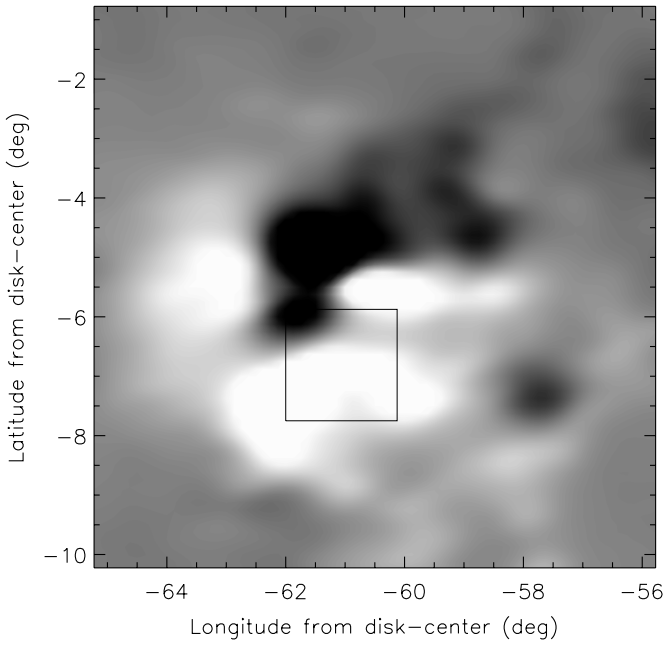

Figure 3. Remapped image of the longitudinal magnetic field of AR10930 based on 10 GONG images immediately preceding the X6.5 flare observed on 2006 December 6th at 1829 UT. The black square corresponds to the pixels featured in the mosaic plot in Figure 5.

c) in Figure 4. In the mosaic, the neutral line appears as a swath of plots without well-defined stepwise changes, extending from the southeast corner to the northwest corner of the mosaic. This swath separates a contiguous region of positive field changes in the northeast, whose boundary is marked with a red line, and a contiguous region of negative changes in the southwest, whose boundary is marked with a blue line. The positive changes above the left part of the red line are significantly stronger than anything reported in SH05. There is also a large, contiguous group of beautiful, low-noise field changes in the bottom right of the mosaic. Some plots show spikes because of flare-induced line profile changes; the line goes into emission rather than absorption, resulting in unphysical measurements (Edelman et al. 2004). Examples of this phenomenon include the pixels at the bottom left of the mosaic. The noise is almost all seeing related and its strength is sensitive to local intensity gradients and magnetic field gradients.

4. FIELD CHANGES

The foregoing analysis gives us thousands of stepwise field changes to consider. Field changes were observed in all 77 flares. In order to characterize the field changes, we followed SH05 in selecting a few representative pixels from each of 77 data sets. While two good data sets were available for each of six of the flares, we used only one data set per flare in this analysis. SH05 selected representative pixels by examining by eye over 8000 mosaic plots like the one in Figure 5. This approach on its own is not practical for our larger data set. To simplify this process, we selected for review pixels with the following characteristics: (1) the stepwise change was at least 1.4 times stronger than the pre-flare background noise level, (2) the time series of measurements passed a reduced-χ^2 test, (3) the background field and field-change values were not unreasonably large ($|a| \leqslant 1000$ G, $|2c| \leqslant 350$ G in general), and (4) the field change was complete within 40 minutes. Criterion (3) was very helpful in general in eliminating unconvincing field changes. All pixels passing tests (1)–(4) were then examined by eye and representative pixels chosen. As Figure 5 shows, the clarity of the field changes varies greatly. In some pixels, the field change is complicated by background noise and by spikes in the data due to an emission feature in the spectral line during the flare. For each active region, we tried to represent every significant sub-region of changing flux and to choose the pixels with the strongest, clearest permanent changes free of noise and emission artifacts. As in SH05, the representative "pixels" are actually averages of the four neighboring pixels that best represent the abruptness and significance of the field change. The resolution of the GONG magnetograms is about 5″, hence an average of four adjacent pixels best represents the true resolution of the data. We also examined the field changes stronger than 350 G by eye and found two sites, one near the 2004 July 16 flare and the other near the 2006 December 6 flare, where such strong-field changes clearly took place. Representative pixels from these two extreme cases appear in Figure 6. Cases with $|a| > 1000$ G existed in our data set but none was convincing enough to include. As in SH05, regions in which the background field strength is greater than 1000 G are too noisy for the clear detection of permanent field changes.

In all, we selected 159 representative pixels from the 77 data sets, compared to 43 pixels representing 15 flares in SH05. The smaller pixel/flare ratio in this study is due to the inclusion of active regions with simpler magnetic structure. For example, if only a single magnetic polarity changed significantly during a given flare we only chose one pixel to represent it (as occurred in four cases of SH05—see their Figure 3). SH05's sample spanned 2001–2003 and featured several very complex active regions. Many of the active regions in this study were bipolar, and showed bipolar changes, bringing our pixel/flare ratio closer to 2.

In each case, the field change is permanent in so far as it persists until the end of the time series. In the vast majority of cases, the time series ends 2 hr after the *GOES* start time of the flare. In some cases, the instrument unstowed or stowed within the 4 hr time interval centered on the *GOES* start time of the

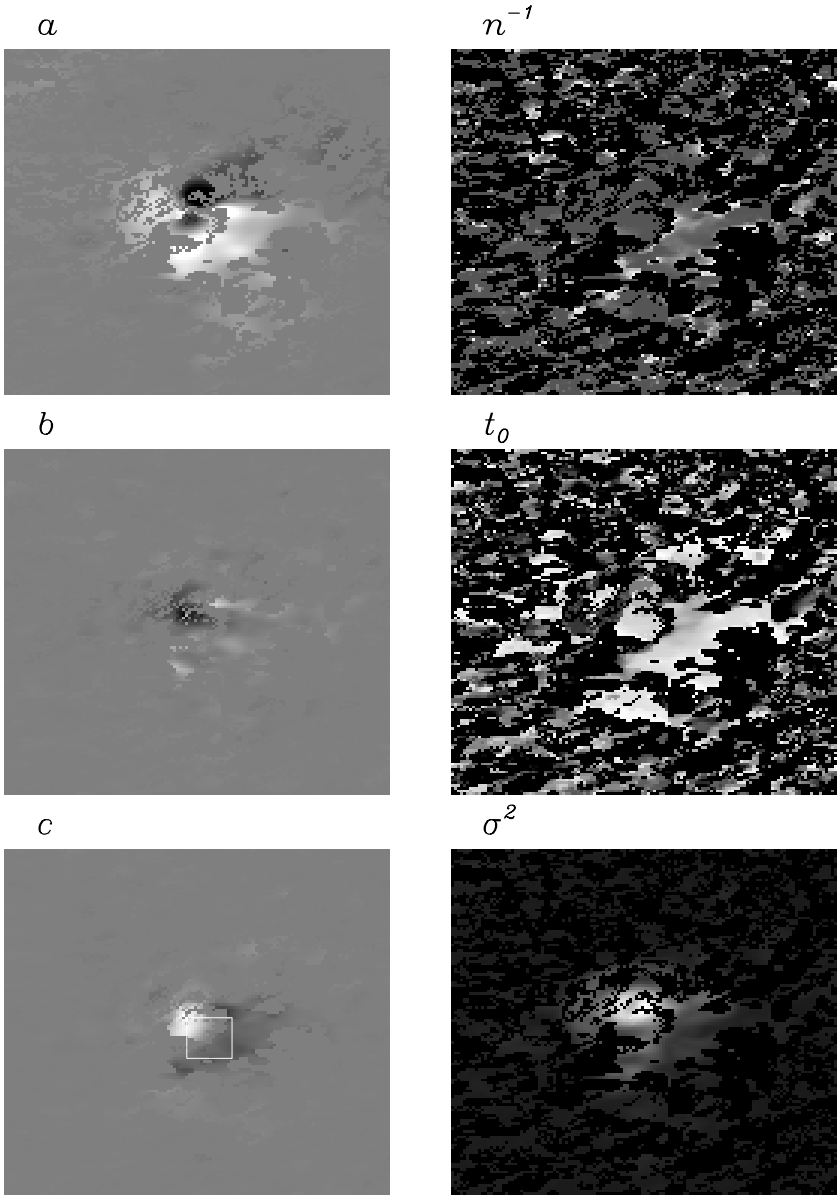

Figure 4. Shown are parameter maps, cropped to 128 × 128 pixels, of the fit parameters a, b, and c (left column, top to bottom) and n^{-1} and t_0 (right column, top and middle) for the X6.5 flare observed on 2006 December 6. The scatter of the data with respect to the fit, σ^2, is shown in the bottom-right panel. Excluded data are represented by gray in the left column and black in the right column. The maps saturate background fields a and abrupt field-changes $2c$ at ±500 G, linear background field evolution b at 2.5 G minute^{-1} and field-change durations πn^{-1} at 20 minutes. Field-change times t_0 range from 100 minutes to 140 minutes and σ^2 from about 0.17 to 1.89. The square in the map for parameter c corresponds to the pixels featured in the mosaic plot in Figure 5.

flare. In all of these cases, the time series extends at least an hour after the field change, and the duration of the field change is much less than an hour. In this sense, all field changes are permanent.

The distributions of the field changes are shown at the top of Figure 7. We will describe the remainder of Figure 7 in Section 5. The significance of a field change is defined as the ratio of the amplitude of the field change to the root-mean-square scatter of the data with respect to the fit before the field change occurred. The top right plot of Figure 7 shows a histogram of this quantity. The minimum in the significance plot is due to the fact that we reject field changes with amplitudes less than 1.4 times the noise level, which is around 20 G for strong active fields and around 3 G for quiet fields. In practice, we calculated the noise level for each pixel under consideration. The histograms suggest power laws.

Figure 8 shows cumulative histograms of the time periods over which the field changes occur, πn^{-1}, for the X-class and M-class flares separately and for all of the flares combined. Because the temporal resolution of the data is 1 minute, where $\pi n^{-1} < 1.0$ in the fit to the data, we reset πn^{-1} to 1.0 in constructing these histograms. This occurs in about 20% of our cases compared to 40% in SH05. The difference is due to the inclusion of slower field changes in this work, up to 40 minutes, compared to the upper limit of 20 minutes in SH05. The time periods over which the field changes occur do not differ significantly between X- and M-class flares. The median value for the X-class flares is 13 minutes whereas the median value for the M-class flares is 15 minutes. (The median value for all flares is 14 minutes.)

The second plot of Figure 8 shows cumulative histograms of the differences between the *GOES* start times of the flares and

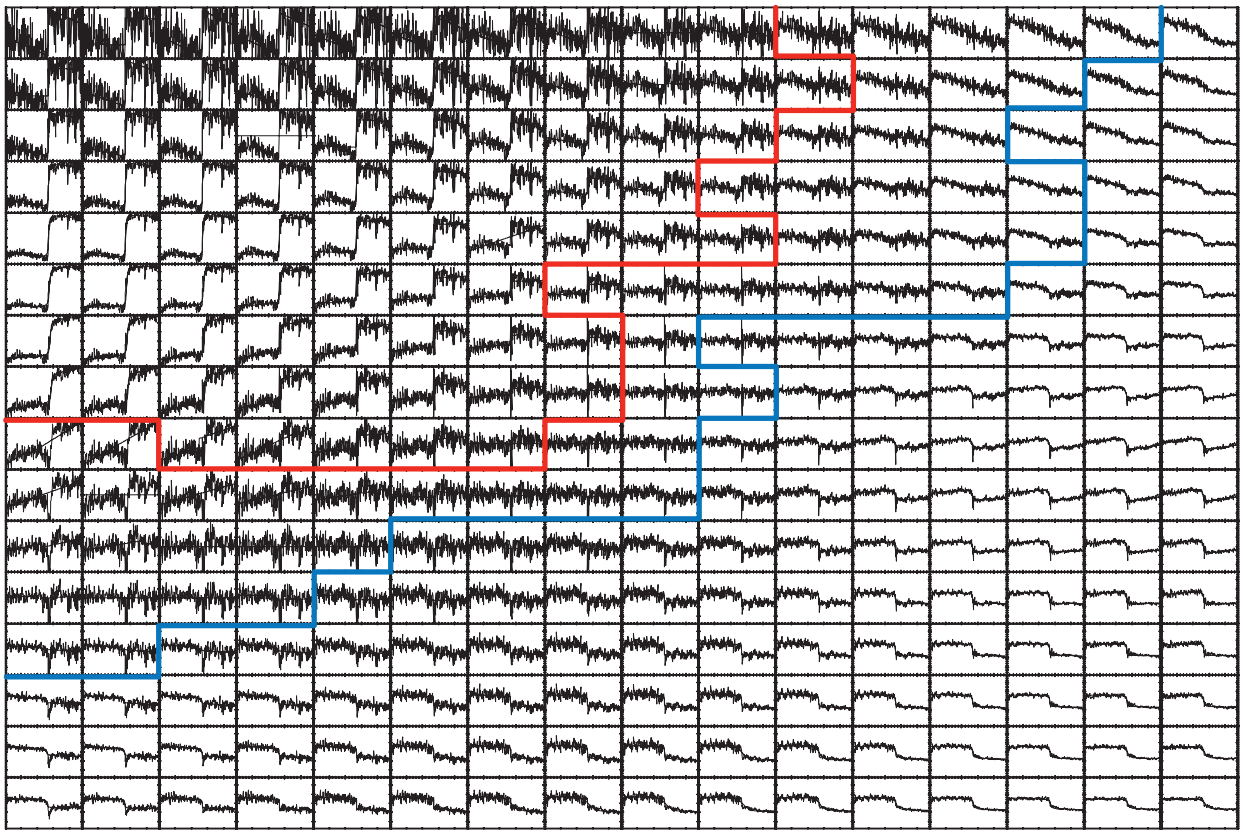

Figure 5. Mosaic of plots of field strength against time for a 16 × 16 pixel subset of the flaring active region 10930 on 2006 December 6 at 1829 UT. This subset of pixels is indicated by the white solid-line square in the *c*-parameter plot in Figure 4. Each plot in the mosaic corresponds to a single pixel. The horizontal axis is time and spans 4 hr. The vertical axis is field strength with its mean value subtracted and spans 500 G. The red and blue lines mark the boundaries of contiguous regions of positive and negative field changes. The swath of pixels between the red and blue lines has no significant stepwise field change.

the start times of the corresponding magnetic field change for X-class and M-class flares separately and for all of the flares combined. The start time, t_s, of the field change is derived from the fit parameters,

$$t_s = t_0 - \pi/(2n), \tag{4}$$

and the time delay, t_d, is the time lag between the *GOES* X-ray start time of the flare (given in Tables 1 and 2) and the start time of the field change, t_s. In about one-third of the cases, the time delays are negative, so it appears that the magnetic field begins to change before the flare occurs. We emphasize again that Equation (1) does not represent a physical model. We do not believe that the negative time delays in the second plot in Figure 8 are meaningful. The start time of the field change, defined by Equation (4), corresponds to the first point of maximum curvature in the step function fit to the data. The longer the time period over which the field change occurs, the shallower the maximum curvature, and the less certain we can be about the time at which the magnetic field begins to change (see Figure 6 for two contrasting examples). Moreover, Equation (1) can represent some measured field changes better than others. For example, if a field change has instantaneous transitions from a constant field to a steady change (straight, sloping graph) to a constant field again, then Equation (1) is doomed to overestimate the field-change duration and the estimated start time, t_s, is too early. This type of error can occur for both abrupt and gradual field changes but is generally larger for gradual changes. In other words, the uncertainty in t_s is proportional to the field-change duration πn^{-1}. Indeed, in our calculations the error in t_s is dominated by the error in n^{-1}, whose 1σ value is often on the order of a few minutes. The third plot in Figure 8 shows the time period over which the field change occurs, πn^{-1}, against the time delay, t_d. The vertical line separates the field changes that appear to start before the *GOES* X-ray signature ($t_d < 0$), at least according to the fit of Equation (1) to the data, and the field changes that start after the *GOES* X-ray signature ($t_d > 0$). The negative time delays are associated with field changes that occur over long periods of time, more than 10 minutes in most cases. They occur in proportionally more cases in this study than in SH05 because we include more gradual changes in our data set. Furthermore, the larger the negative time delay, the longer the duration of the field change. The negative time delays appear to be an artifact. We maintain that the magnetic field changes are a consequence of solar flares and not a trigger.

Figure 9 shows a scatter plot of the magnetic field changes, dB_l, against background field intensities, B_l, for all of the representative pixels in our data set. The empty, narrow, horizontal stripe represents our detection limit. Two notable exceptions appear at −455 and +445 G, recorded during the 2004 July 16 X3.6 flare and the 2006 December 6 X6.5 flare, respectively. Although the parameters of the fits to the time series plots associated with these field changes fall outside our normal criteria for inspection, field changes stronger than 350 G are quite rare, so we were able to examine all of the representative pixels for which $|2c| > 350$ G by eye. In doing so, we found these two extreme cases, which we present in Figure 6. Apart from these two extreme cases, the distribution of field changes between −300 G and +300 G is consistent with SH05, though we did find field changes as weak as 11 G compared to 28 G in SH05.

Table 3
Maximum, Minimum, and Median Absolute Field Changes

Flare Category	Minimum Change (G)	Maximum Change (G)	Median Change (G)
All flares	11	455	69
X-class flares	11	455	82
M-class flares	13	236	54
Disk-center flares	13	281	54
Limb flares	11	455	85
Disk-center X-class flares	16	281	71
Limb X-class flares	11	455	97
Disk-center M-class flares	13	149	44
Limb M-class flares	13	266	69

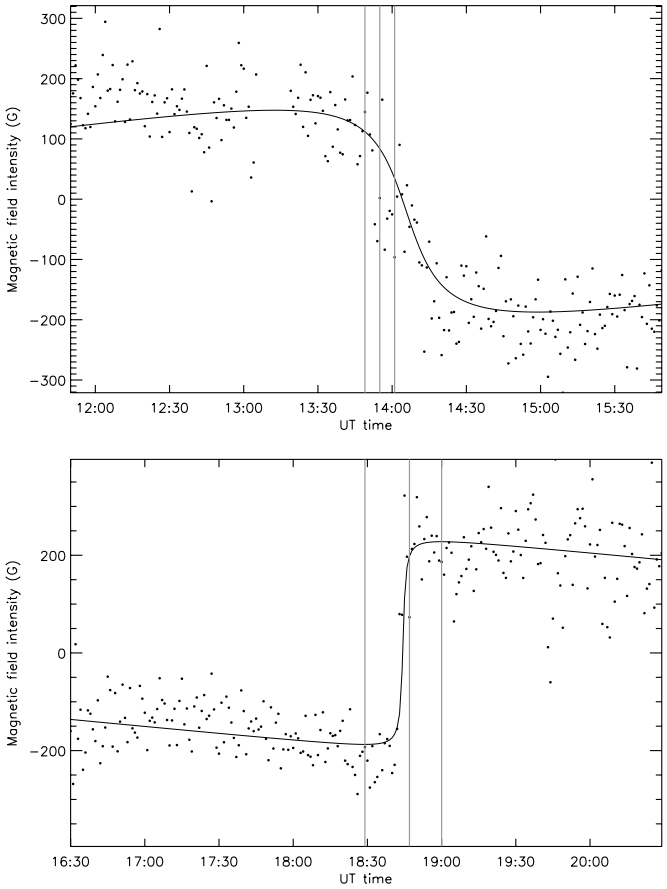

Figure 6. Observational data points and fitted curves for the two strongest field changes in our sample recorded during the 2004 July 16 X3.6 flare (top) and the 2006 December 6 X6.5 flare (bottom). The mean value of magnetic field intensity has been subtracted from the data and the fit in each plot. The vertical lines mark the *GOES* X-ray start, peak, and end times of the flares.

In Table 3, we summarize the maximum, minimum, and median of the absolute values of the field changes for all of the representative pixels and for different subsets of the data. The absolute values of all of the field changes range from 11 G to 455 G with a median value of 69 G. Field changes associated with X-class flares have a median value of 82 G, close to the median value of 90 G reported in SH05, while the M-class flares have a lower median value of 54 G. SH05 found no correlation between the strength of the field change and position on the solar disk. Here, however, we do find a split in the data between field changes near the limb and near disk center. In this paper, we denote by "near disk center" those locations where $r \leqslant r_s/2$ and by "near the limb" those where $r > r_s/2$ (see Figure 1), where r_s is the solar disk radius in the image plane. Field changes near the limb have a higher median value, 85 G, than field changes near disk center, 54 G. Although there are more X-class flares than M-class flares at the limb, the X-class and limb-flare biases are independent. The median field change for limb X-class flares, 97 G, is significantly higher than both the median disk-center X-class change, 71 G, and the median limb M-class change, 69 G, which are both in turn significantly higher than the median disk-center M-class change, 44 G.

SH05 reported that field changes are twice as likely to decrease the field as increase it. More precisely, 27 of the 42 observed changes in the longitudinal magnetic field were associated with a decrease in the background field intensity, whereas 15 were associated with an increase, a ratio of 1.8–1. In Table 4, we present the statistics for decreasing/increasing fields. Of the 159 field changes in our study, 94 decreased the field while 65 increased it, a ratio of 1.4–1, lower than in SH05. The asymmetry is apparent in Figure 9; the top left and bottom right quadrants are more populated than the top right and bottom left quadrants. This figure also shows a difference between the shapes of the distributions of changes with size greater than and less than 100 G. Note also the sharp drop-off at 100 G in the first panel of Figure 7. We find that weak-field changes, $|dB_l| < 100$ G, are nearly twice as likely to decrease the field as increase it (row 4 in Table 4). This bias is greater near disk center, where increases are more than twice as numerous as decreases, than near the limb (compare rows 8 and 10 in Table 4). On the other hand, strong-field changes, $|dB_l| > 100$ G, are slightly more likely to increase the field (rows 5, 9, and 11 in Table 4). So the split in decreasing/increasing fields is dominated by weak-field changes and is strongest near disk center.

In Table 4, we also present the Pearson correlation coefficient, r_0, between the field change, dB_l, and the background field intensity, B_l, for all of the representative points and for different subsets of the data. We include in Table 4 the probability, $P(|r| > |r_0|)$, that the same number of measurements of two uncorrelated variables would yield a correlation coefficient $r > r_0$. Overall, we find no correlation between the field changes and the background field intensities (row 1 in Table 4), consistent with SH05, but we do find that weak-field changes, $|dB_l| < 100$ G, show a modest negative correlation with background field intensity both near disk center and near the limb but the correlation is stronger near disk center (rows 4, 8, and 10 in Table 4).

5. FLUX CHANGES

As SH05 have noted, the change in magnetic flux may be a more important physical quantity than the most significant and abrupt field change at one particular location. The representative pixels represent the fastest and strongest field changes, free of

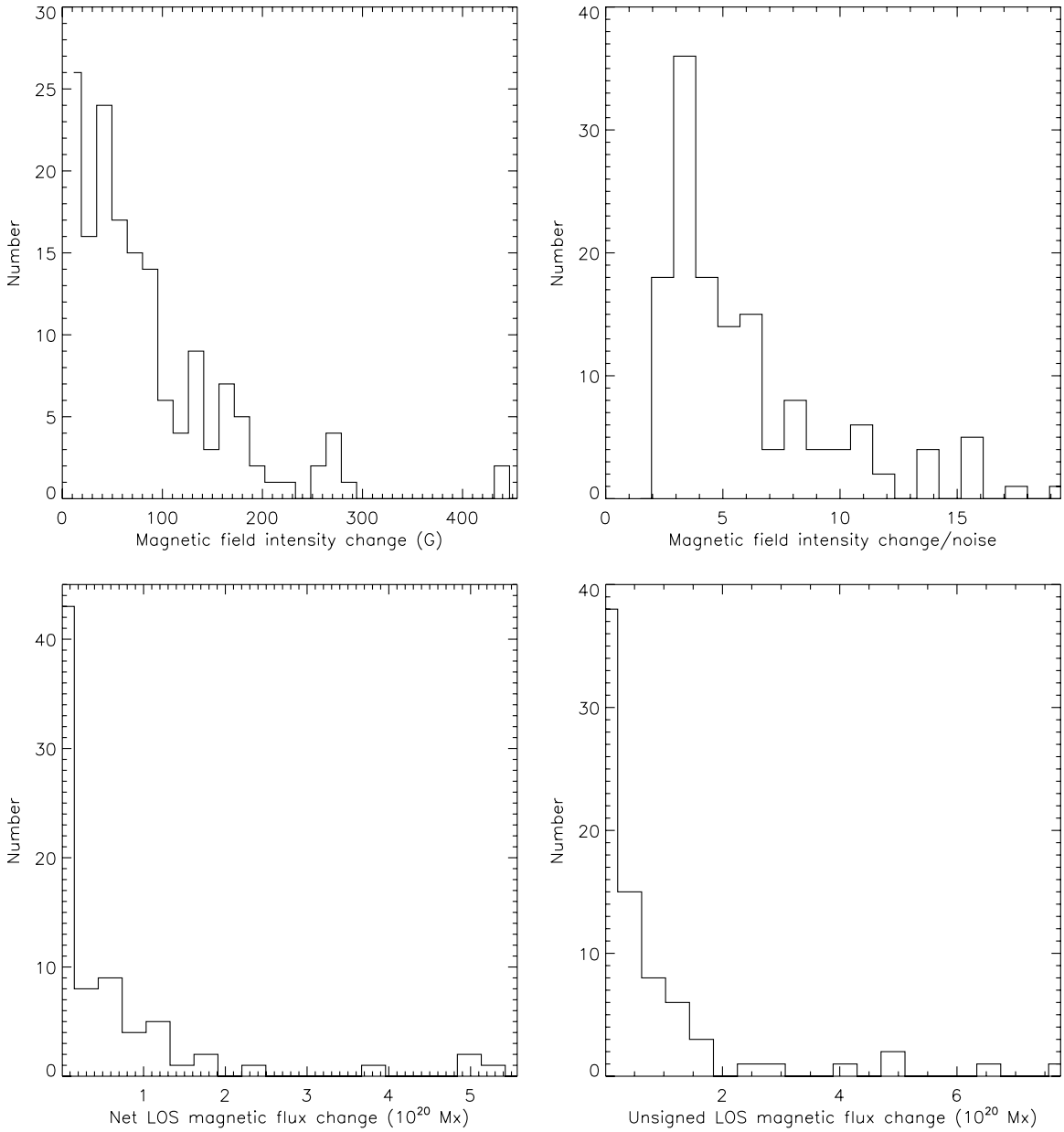

Figure 7. Histograms of field changes (top left), the significance of these field changes (top right), the change in net flux (bottom left), and the change in unsigned flux (bottom right). The significance is defined as the ratio of the amplitude of the field change to the rms scatter in the data with respect to the model before the field change occurs.

Table 4
Field Changes: Selected Statistics, Correlations, and Confidence Levels

Flare Category	No. Fields Increasing	No. Fields Decreasing	Pearson c.c. r_0 Between B_l and dB_l	Probability $\mathrm{Prob}_N(\lvert r\rvert \geqslant \lvert r_0\rvert)$ for N Measurements
All field changes	65	94	−0.035	0.66
X-class field changes	34	56	−0.04	0.71
M-class field changes	31	38	0.01	0.94
Weak-field changes	37	71	−0.43	2.4×10^{-6}
Strong-field changes	28	23	0.20	0.17
Disk-center field changes	23	42	−0.20	0.11
Limb field changes	42	52	0.037	0.72
Weak disk-center field changes	17	36	−0.51	6.9×10^{-5}
Strong disk-center field changes	6	6	0.37	0.34
Weak limb field changes	20	35	−0.37	5.1×10^{-3}
Strong limb field changes	22	15	0.27	0.24

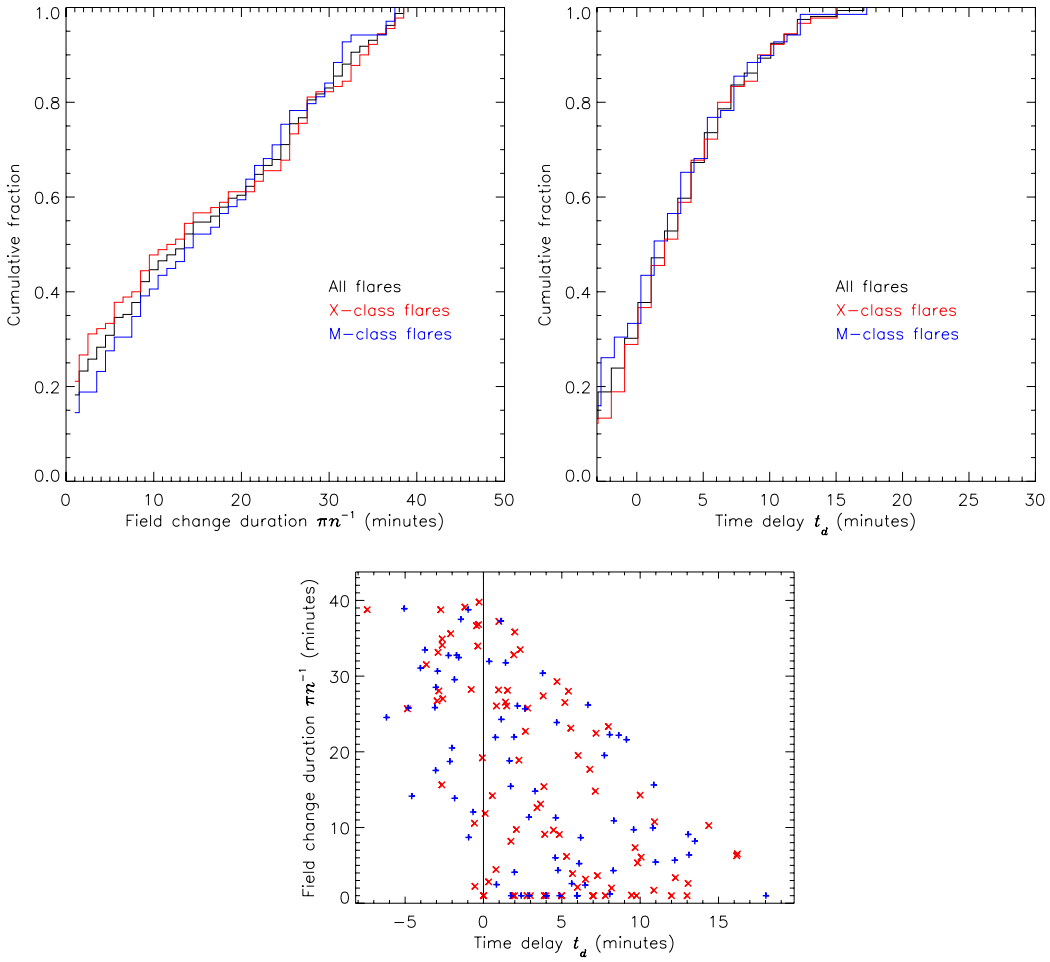

Figure 8. Cumulative histograms of the time periods over which the magnetic field changes occur πn^{-1} (top left), cumulative histograms of the time delays between the start times of the *GOES* X-ray flare signatures and the magnetic field changes for the X-class and M-class flares separately and all flares combined (top right), and a scatter plot of the time periods over which the field changes occur against time delays (bottom). In the scatter plot, blue plus signs (+) denote M-class flares and red crosses (×) X-class flares. The vertical line separates cases where the field-change start time, derived from the fit of Equation (1) to the data, lags ($t_d > 0$) and leads ($t_d < 0$) the published *GOES* X-ray flare start time.

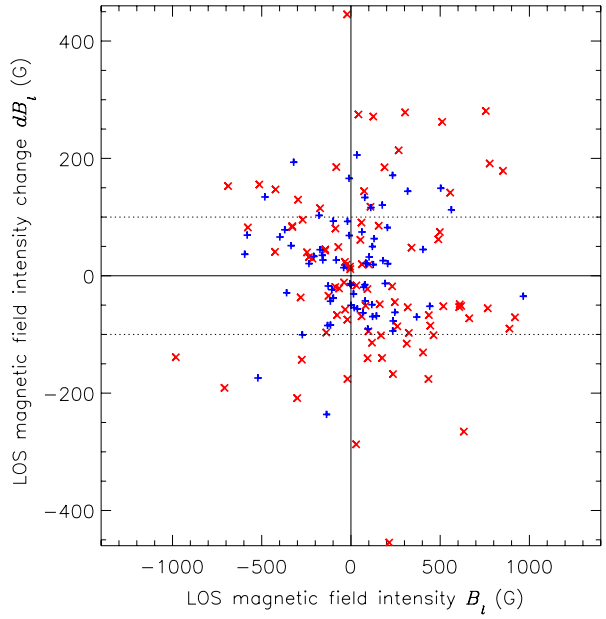

Figure 9. Scatter plot of the longitudinal field changes, dB_l, against the background field values, B_l. Blue plus signs (+) denote M-class flares and red crosses (×) X-class flares. The dotted lines separate weak-field changes ($|2c| \leqslant 100$ G) and strong-field changes ($|2c| > 100$ G). The former are negatively correlated with background field while the latter are not.

artifacts, but do not present a complete picture of the changes to the magnetic field in an active region. Magnetic flux calculations capture the effects of flares on entire active regions. In this section, we estimate the change in the magnetic flux during each flare. Because all of the pixels in a remapped image have equal area, the net flux is just the sum of the field changes over all of the pixels in the remapped image. We eliminate from consideration, of course, those pixels for which the parameters of the fit of Equation (1) to the time series plot do not satisfy all of the criteria (1)–(4) described in Section 4. These flux calculations no doubt include some "false positives," but we expect these to average out.

Figure 7 shows histograms of the net (bottom left) and unsigned (bottom right) magnetic flux changes for all 77 flares in this study. The vast majority of the flux changes are toward the weak end of the scale. About half of the flares fall into the first bin in each histogram. Like the histogram of field changes in the same figure, these histograms resemble power laws but with a stronger power index. The flux changes have a greater range of values than the field changes do because the area is a varying parameter in the flux calculations but not in the field intensity calculations.

Table 5 shows the statistics for the increases and decreases in net and unsigned flux. The net fluxes increase in approximately equal numbers in general (compare the first two columns of

Table 5
Increasing and Decreasing Net and Unsigned Magnetic Fluxes

Flare Category	No. Net Increasing	No. Net Decreasing	No. Unsigned Increasing	No. Unsigned Decreasing
All	37	40	29	48
X-class	19	19	12	26
M-class	18	21	17	22
Disk center	14	18	12	20
Limb	23	22	17	28
Disk-center X-class	7	5	3	9
Disk-center M-class	7	13	9	11
Limb X-class	12	14	9	17
Limb M-class	11	8	8	11

Table 5). Unsigned fluxes, on the other hand, decrease for nearly two-thirds of the flares overall (see the top row of Table 5), and for those near disk center as well as those near the limb (rows 4 and 5 of Table 5). For X-class flares, the ratio of flux decreases to increases is greater than 2:1 while for M-class flares the ratio is closer to 1:1 (compare rows 2 and 3 of Table 5). X-class flares near disk center show three times as many decreases as increases in unsigned flux whereas X-class flares near the limb show fewer than twice as many (rows 6 and 8 of Table 5). The corresponding M-class statistics are closer to 1:1, perhaps because they are compromised by noise (rows 7 and 9 of Table 5). When we sort the data according to location, east/west or north/south or quadrants, no patterns emerge.

Wang & Liu (2010) found for 17 out of 18 flares occurring in δ-spots that the limbward flux increased and the diskward flux decreased according to longitudinal field measurements. It is not straightforward to compare these results with ours because the active regions in our data set do not generally have bipolar flux distributions, and those that do are not always aligned approximately east–west.

Figure 10 shows the scatter plots of net and unsigned flux change against background net and unsigned flux. The correlations between magnetic flux changes and background flux are summarized in Table 6. The statistics show a significant overall (negative) correlation between the net magnetic flux changes and the net background fluxes. This contrasts with the overall result for field changes in row 1 of Table 4. Figure 10 (left panel) also shows this overall negative correlation between net fluxes and net flux changes. The distribution shown in this figure is very different from the corresponding distribution of field changes shown in Figure 9. Although only slightly more net fluxes decrease than increase, the larger net flux changes generally decrease, hence the significant correlation between the net and unsigned flux change and the net and unsigned background flux (row 1 in Table 6). Furthermore, the larger flux changes are almost all associated with X-class flares, so the negative correlation is significant for X-class examples but not for M-class examples (compare rows 2 and 3 in Table 6). There is stronger correlation near the limb than near disk center (compare rows 4 and 5 in Table 6). X-class flares show stronger correlation near the limb than near disk center (rows 6 and 8 in Table 6). This is because the largest flux changes occur during X-class flares near the limb, a phenomenon that we will discuss further in Section 7. On the other hand, among M-class flares disk-center cases show significant correlation with a 95% confidence level while limb cases do not (rows 7 and 9 of Table 6). This may be because more of the M-class data near the limb are compromised by noise.

Table 6
Pearson Correlation Coefficients and Confidence Levels for Magnetic Flux Changes Against Magnetic Flux

Flare Category	Pearson c.c. r_0 Net Flux	Probability $P(\lvert r\rvert \geqslant \lvert r_0\rvert)$	Pearson c.c. r_0 Unsigned Flux	Probability $P(\lvert r\rvert \geqslant \lvert r_0\rvert)$
All	−0.62	4.5×10^{-10}	0.70	8.6×10^{-14}
X-class	−0.66	2.7×10^{-6}	0.76	3.8×10^{-9}
M-class	−0.15	0.36	0.26	0.11
Disk center	−0.46	7.4×10^{-3}	0.66	2.0×10^{-4}
Limb	−0.68	7.7×10^{-8}	0.80	1.1×10^{-12}
Disk-center X-class	−0.50	9.9×10^{-2}	0.74	4.3×10^{-3}
Disk-center M-class	−0.46	4.0×10^{-2}	0.43	5.8×10^{-2}
Limb X-class	−0.72	1.3×10^{-5}	0.82	2.9×10^{-8}
Limb M-class	0.063	0.80	0.29	0.23

6. RELATION OF FIELD AND FLUX CHANGES TO *GOES* PEAK X-RAY FLUX

We have seen that correlations of changes in field intensity or flux with their background values are different for *GOES* X-class and M-class flares and for flares observed near the limb and near disk center. Photospheric magnetic field properties have often been explored in the past as possible predictors of flare activity. For example, the estimated unsigned radial magnetic flux of the active region and the unsigned flux near strong-field polarity inversion lines are two magnetic quantities that have been found to correlate with *GOES* X-ray flare flux (Leka & Barnes 2007; Schrijver 2007; Welsch et al. 2009). In this section we seek correlations between the detected longitudinal magnetic field and flux changes and *GOES* X-ray flare flux.

Figure 11 shows scatter plots of the magnetic field intensity changes and the net and unsigned magnetic flux changes against the *GOES* peak X-ray flux. Table 7 summarizes the correlations between the field and flux change and the *GOES* peak X-ray flux. Overall, the field change, the net flux change, and the unsigned flux change all show some weak to moderate correlation with *GOES* X-ray flux (row 1 of Table 7). The correlation between field change and *GOES* X-ray flux is dominated by X-class flares at the limb (compare the first two columns of rows 2, 5, and 8 in Table 7). As discussed in Section 4, the median value of the field change is higher for X-class flares than for M-class flares and for limb flares than disk-center flares (Table 3). All this adds up to the conclusion that X-class limb flares are slightly more likely than other flares to produce strong longitudinal field changes.

Some correlation between the change in the magnetic flux and the *GOES* X-ray flux is expected, as discussed in Section 5, and the correlation is dominated by the X-class flares (compare rows 1 and 2 in Table 7). The statistically significant correlation between the net magnetic flux change and the *GOES* X-ray flux at disk center is dominated by the disk-center X-class flares (compare the middle two columns of rows 4 and 6 in Table 7). The statistically significant correlation between the unsigned magnetic flux change and the *GOES* X-ray flux near the limb is dominated by the limb X-class flares (compare the last two columns of rows 5 and 8 in Table 7), so the X-class flare theme repeats itself, but we do see two deviations from this theme. The correlation between the net flux change at the limb and the *GOES* X-ray flux (middle two columns of line 5) appears to be split amongst X- and M-class flares (rows 8 and 9). The correlation between the unsigned magnetic flux change and *GOES* X-ray flux near disk center (last two columns of line 4) appears to be significant in spite of the fact that the separate M-class and

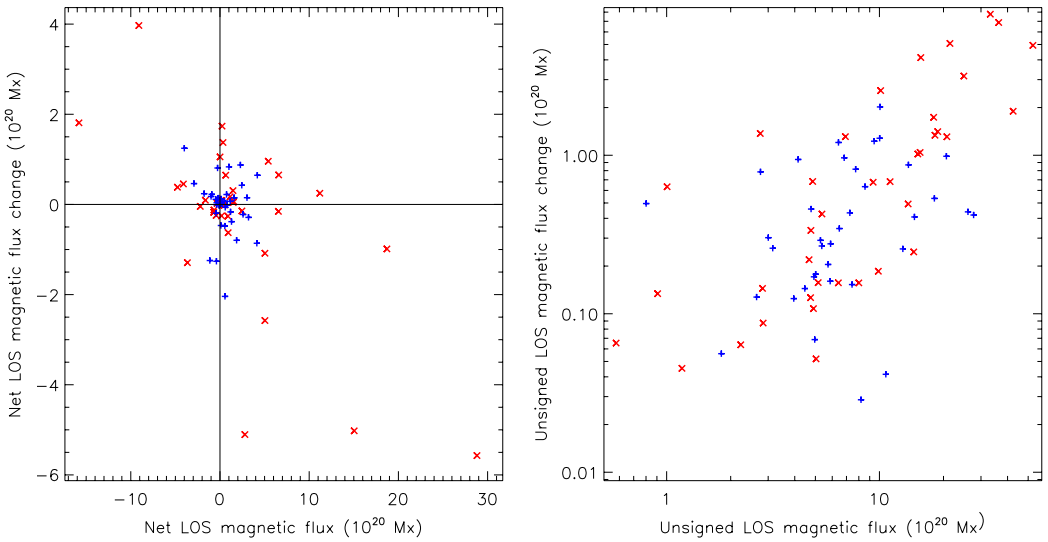

Figure 10. Scatter plots of the change in the net magnetic flux against the background net magnetic flux (left) and the change in the unsigned magnetic flux against the background unsigned magnetic flux (right). Blue plus signs (+) denote M-class cases and red crosses (×) X-class cases.

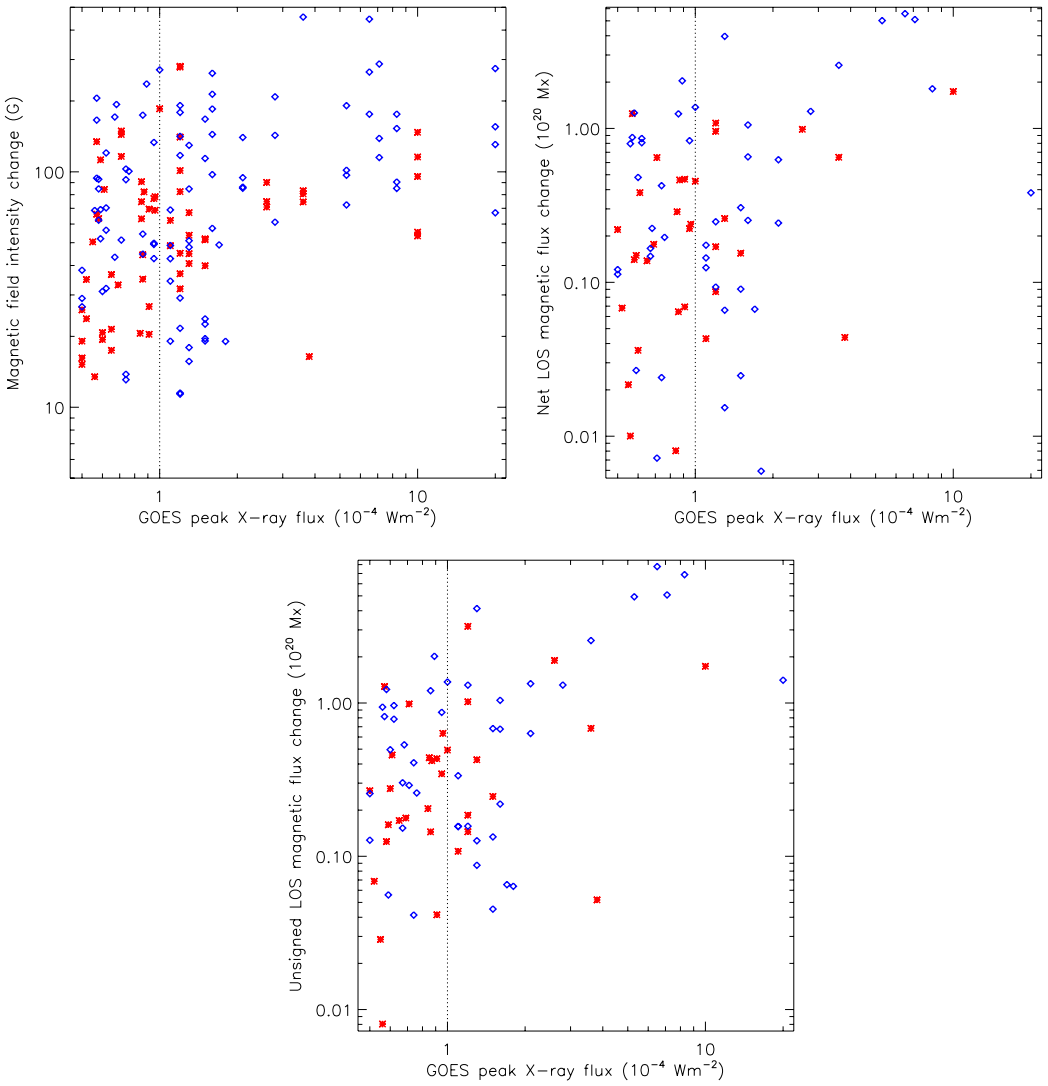

Figure 11. Scatter plots of magnetic field change (top left), change in net magnetic flux (top right), and change in unsigned magnetic flux (bottom) against *GOES* peak X-ray flux. *GOES* peak X-ray flux values < 1 (left of dotted line) correspond to M-class flares while values $\geqslant 1$ (dotted line and above) correspond to X-class flares. Red asterisks (*) denote flares with radial position $r \leqslant r_s/2$ on the solar disk, and blue diamonds ($\diamond$) denote cases with $r > r_s/2$, where r_s is the solar disk radius in the image plane.

Table 7
Pearson Correlation Coefficients and Confidence Levels of Field and Flux Changes with *GOES* Peak X-ray Flux

Flare Category	Pearson c.c. r_{bi} Field Intensity Change	Probability $P(\|r\| \geqslant \|r_{bi}\|)$	Pearson c.c. r_{ni} Net Flux Change	Probability $P(\|r\| \geqslant \|r_{ni}\|)$	Pearson c.c. r_{ui} Unsigned Fux Change	Probability $P(\|r\| \geqslant \|r_{ui}\|)$
All	0.28	3.3×10^{-4}	0.38	5.7×10^{-4}	0.48	6.8×10^{-6}
X-class	0.22	3.7×10^{-2}	0.32	5.0×10^{-2}	0.42	8.1×10^{-3}
M-class	0.25	0.14	0.14	0.40	0.18	0.27
Disk center	0.14	0.27	0.60	1.8×10^{-4}	0.37	3.6×10^{-2}
Limb	0.29	4.4×10^{-3}	0.34	2.2×10^{-2}	0.49	5.1×10^{-4}
Disk-center X-class	−0.01	0.96	0.65	2.0×10^{-2}	0.25	0.44
Disk-center M-class	0.22	0.21	0.00	1.00	0.11	0.65
Limb X-class	0.26	4.5×10^{-2}	0.29	0.15	0.43	2.7×10^{-2}
Limb M-class	0.12	0.50	0.38	0.11	0.39	0.10

X-class correlations are not. This is because these distributions occupy disjoint parts of the parameter space. For limb flares, the overall correlation (row 5) is stronger than the separate X-class and M-class correlations (rows 8 and 9) for the same reason.

We see a more significant correlation between net flux change and *GOES* X-ray flux at disk center than at the limb (but both correlations have a confidence level better than 5%) and a more significant correlation between unsigned flux change and *GOES* X-ray flux at the limb than at disk center (but again both correlations have a confidence level better than 5%). A large net flux change implies a large asymmetry between the change in positive flux and the change in negative flux. If the net flux change is large then positive and negative fluxes cannot both have moved toward or away from zero by approximately the same amount. Therefore, the fact that net flux changes correlate well with peak *GOES* X-ray flux near disk center suggests a connection between X-ray flux emission and asymmetric vertical flux changes.

7. RELATION OF FIELD AND FLUX CHANGES TO THEIR POSITION ON THE SOLAR DISK

SH05 reported that they found no trends when they sorted their data by hemisphere or by distance from disk center. While we do not see significant differences between the hemispheres in our larger data set, we have seen in Section 4 that the median field change near the limb is greater than the median value near disk center. In this section, we investigate directly the relationship between the distance from disk center and the size of changes in magnetic field intensity and flux.

Figure 12 shows scatter plots of changes in magnetic field intensity (top left), net flux (top right), and unsigned flux (bottom) against radial position on the solar disk. The top-left plot clearly shows that strong-field changes occur preferentially closer to the limb than to disk center. Indeed, when we sort and bin the field changes in terms of radial position on the disk in three equally populated bins, the averages and standard deviations of these bins are 32.4 ± 126.1 G, -18.1 ± 168.2 G, and 25.0 ± 206.7 G. The distributions therefore become wider with increasing radial distance from disk center. A larger range of longitudinal field changes is found near the limb than near disk center. If we exclude the two strongest field changes, one of which falls into the middle bin and the other into the limbward bin, the averages remain small and the standard deviations still increase toward the limb. It is clear that the strongest longitudinal field changes occur close to the limb. Therefore, the strongest changes occur in cases whose observed field component is nearly horizontal.

Net flux changes show similar spatial dependence. The top right picture of Figure 12 shows that only rather weak net flux changes are found close to disk center while the range of flux changes increases with increasing distance from disk center. The strongest net flux changes are concentrated close to the limb. One interpretation of this pattern is that there is simply more longitudinal flux changing near the limb than near disk center because most of this flux is nearly horizontal. This interpretation is supported by the spatial distribution of unsigned flux changes. According to the bottom picture in Figure 12, the unsigned longitudinal flux changes by large quantities near the limb but not near disk center. All told, the data suggest that the photospheric fields that undergo the greatest change as a result of flares are nearly horizontal. Such structures might include low-lying loops across neutral lines or in sunspot penumbrae.

8. FORCES AND ENERGETICS OF THE FIELD CHANGES

In this section, we estimate the Lorentz forces applied to the photosphere by the coronal field using the photospheric magnetic field measurements. Following a pioneering calculation by A. N. McClymont (Anwar et al. 1993; Hudson et al. 2008; Fisher et al. 2010), we can estimate how much of the released flare energy goes into reorganizing the photospheric field. Assuming that the photosphere was in force-balanced equilibrium before the flare, a known vector field change of $(\delta B_x, \delta B_y, \delta B_z)$ results in a force imbalance whose vertical component would be

$$\delta f_z = (B_z \delta B_z - B_x \delta B_x - B_y \delta B_y)/4\pi. \quad (5)$$

The total vertical force on the photosphere could then be found by integrating δf_z over the area over which field changes occur. Fisher et al. (2010) show that this expression should give a robust and accurate estimate if integrated over regions of strong field in a vector magnetogram and if the field changes are small compared to the initial field values. Since here we only have longitudinal measurements we estimate the size of force change by

$$\delta f_l = B_l \delta B_l / 4\pi. \quad (6)$$

Figure 13 shows a scatter plot of these force estimates against the *GOES* peak X-ray fluxes. The width of the distribution increases as a function of *GOES* peak X-ray flux. The largest forces correspond to major X-class flares while no M-class flare produces a force stronger than about 3×10^{21} dynes. Only one term (out of three) of the expression for the Lorentz force in Equation (6) is available from longitudinal data, so the sign of the force is not determined by a single field component. On the other hand, we can say from the sign of Equation (6) whether

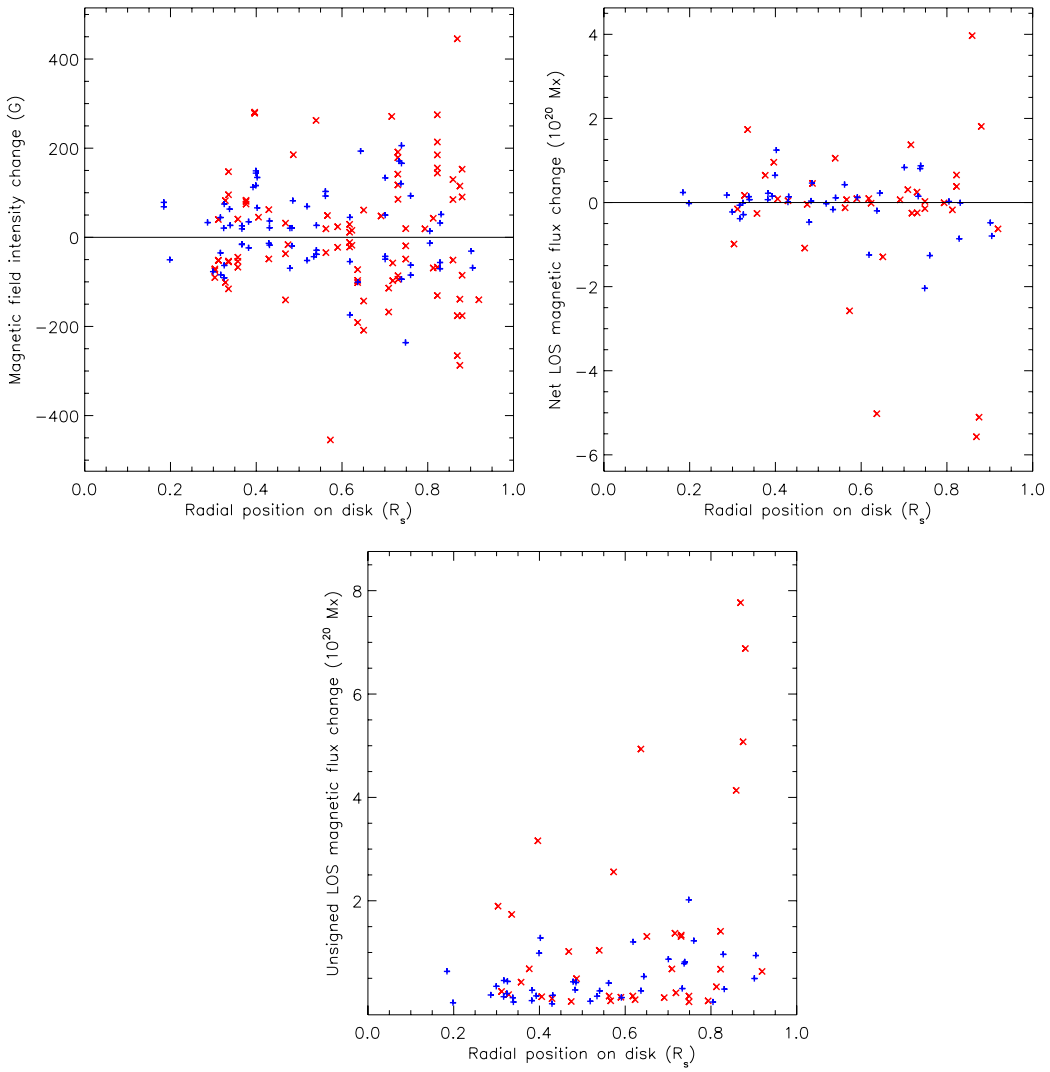

Figure 12. Scatter plots of the change in magnetic field intensity (top left) and the net (top right) and unsigned (bottom) magnetic flux changes against radial position on the solar disk. Blue plus signs (+) denote M-class cases and red crosses "×" X-class cases.

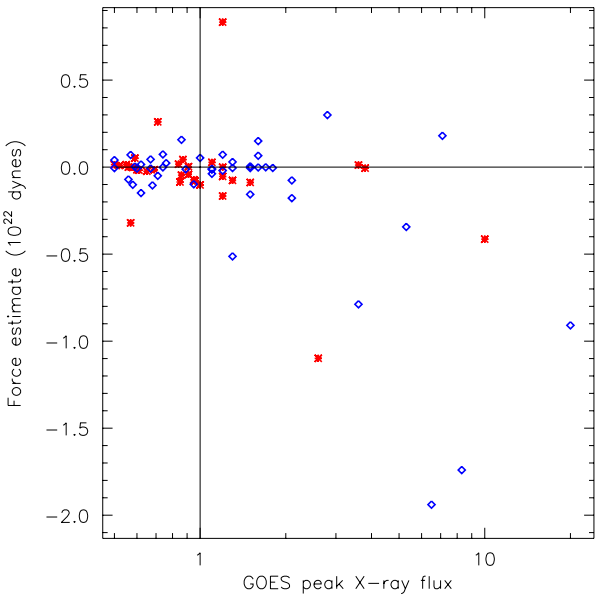

Figure 13. Scatter plot of Lorentz force estimates against *GOES* peak X-ray flux. Red asterisks (*) denote flares with radial position $r \leqslant r_s/2$ on the solar disk, and blue diamonds (⋄) cases with $r > r_s/2$, where r_s is the solar disk radius in the image plane.

B_l increased or decreased in strength. There are 27 positive force values and 50 negative, meaning that more of the fields decreased than increased. As for the largest forces of size greater than 5×10^{21} dynes, there are six associated with decreasing fields and one associated with an increasing field. The largest forces in the sample are associated with decreasing fields. The fact that $B_l \delta B_l$ is more likely to be negative than positive is consistent with the results of Sections 4 and 5. Confirmation with a full force estimate must await a sizable sample of good, high-cadence vector data. Hudson et al. (2008) estimated that forces of size 10^{22} dynes can be important for the physics of seismic waves. Several examples in Figure 13 have force budgets of this size. Given that the forces calculated here involve only those pixels well modeled by Equation (1), some of these forces might be significantly underestimated. Recently, Wang & Liu (2010) applied Equation (5) to a BBSO vector data set for the 2002 July 26 M8.7 flare and found a vertical force change of 1.6×10^{22} dynes. Our estimated force change for the 2002 July 26 M8.7 flare using Equation (6) is 4.3×10^{21} dynes. The difference between the force change estimates from GONG longitudinal data and BBSO vector data is perhaps mostly due to the inclusion of the transverse field in Wang & Liu's calculation. We note, however, that Martínez-Oliveros & Donea (2009) did not find good spatial correspondence between locations of

abrupt, significant field changes and seismic sources in the two flares that they studied.

The most impressive estimated force budget in our data set is for the 2006 December 6 X6.5 flare featured in Figures 3–5. This flare has been associated with a Moreton wave, studied in detail by Balasubramaniam et al. (2010) using Hα images from the Improved Solar Observing Optical Network (ISOON). This Moreton wave traveled from its source at approximately S06E63 at about 800 km s^{-1} with an azimuthal span of about 270°. A blow-up of the east-limb portion of the full-disk magnetogram of Figure 2 is plotted in Figure 14, showing the flaring active region, AR 10930. Also plotted is an ISOON Hα image taken at the height of the flare showing the flare emission. As Figure 14 shows, the estimated central source was rather distant, 35–75 Mm distant according to Balasubramaniam et al.'s estimate, from the centroid of *RHESSI* X-ray and ISOON white-light emission.

This flare was also well observed by the Cerro Tololo station of the GONG network. The data set for this flare has the largest detected number of pixels where large, clean, permanent stepwise field changes were detected of any of the 77 flares studied here, as well as the most impressive force budget. The total forces involved amount to about 2×10^{22} dynes. The spatial distribution of the changes occurring between 1830 UT and 1850 UT is shown in Figure 15. The forces are organized in two regions, a small region of relatively weak forces close to the neutral line mostly directed toward the observer (positive) and a more extended region to the south and west of somewhat larger forces directed toward the Sun (negative). (Note that in this example the line of sight is tilted at 60° with respect to the local vertical.) While the group of positive forces is close to the centroid of the X-ray emission, the largest forces are clustered to the west, closer to the location of the focal point of the Moreton wave (see Figure 14). The centroids in Figure 14 show that the changes began near the negative-polarity sunspot and then propagated to the south and west. The field changes associated with the largest forces are located in a region of strong positive magnetic flux a degree or so west of the sunspot. The field changes themselves, at about 270 G, are significantly weaker than the strongest changes during the flare, of about 450 G, that are to be found in the region above the left part of the red line in Figure 5, but their force estimates are larger because they occur in a much stronger field.

Shown in Figure 16 is a simultaneous 10 minute averaged GONG continuum-intensity image, remapped to the same local Cartesian coordinates with the same forces plotted as in Figure 15. This intensity image shows the sunspot structure. Most of the field and force changes appear to fall within the southwestern quadrant of the sunspot penumbra. The inner penumbra has a mixture of field increases and decreases, including the strongest field changes observed during this flare (see Figure 5). The very large contiguous region of field decreases to the southwest follows the outer penumbra, including a relatively intense outer penumbral structure due east of the sunspot where the largest force changes occur.

The 2006 December 6 X6.5 flare exemplifies many of the features characteristic of our data set. The majority of the pixels show longitudinal field decreases while the strongest changes, those nearest the sunspot, are a mixture of longitudinal field increases and decreases. The largest forces are associated with longitudinal field decreases, suggesting a downward collapse. These features are typical for flares both near disk center and, as in this case, near the limb.

The temporal distribution of the inferred longitudinal Lorentz force changes peaked between 1840 and 1845 UT, around the time of the fast acceleration phase of the associated coronal mass ejection (CME; Balasubramaniam et al. 2010). Fletcher & Hudson (2008) give a physical argument relating flare Alfvén waves with permanent photospheric field changes. To our knowledge, no analogous argument for a CME bow shock has been given, but Fisher et al. (2010) argue from Newton's third law that a change in the photospheric field to a more horizontal direction implies an inward impulse toward the solar interior accompanied by an equal and opposite outward force on the solar atmosphere. We have been unable to determine whether or not a seismic wave also occurred during the flare because of the low quality of Doppler images so far from disk center.

9. DISCUSSION

The observations presented in this paper provide information only on the component of the magnetic field along the observer's line of sight. The measured net longitudinal flux generally changes during a flare at a great rate ($\approx 10^{18}$ Mx s^{-1}) and so it seems most likely that the changes in longitudinal field are caused by changes in field direction and not strength (SH05). Proof of this can only come from precise, unambiguous, high-cadence magnetic vector field observations. As we discussed in Section 1, Fletcher & Hudson (2008) have shown that large-scale Alfvén waves might transport enough energy from the flare site rapidly through the corona to change the magnetic field irreversibly at the photospheric level. Related theoretical work (Hudson 2000; Hudson et al. 2008; Fisher et al. 2010) predicts that the flaring photospheric magnetic fields undergo an implosion and become more horizontal as a result of flares. In this section, we assume that the change in the longitudinal field is caused entirely by a change in the direction of the magnetic vector and not by a change in its strength. Then we determine whether our observations are consistent with magnetic field vectors becoming more horizontal under this assumption.

The longitudinal component B_l of the magnetic field is related to the Cartesian components of the field, B_x, B_y, and B_z in local heliographic coordinates and the heliographic latitudinal and longitudinal displacements from disk center, B and L, by the equation (e.g., Hagyard 1987)

$$B_l = B_z \cos B \cos L - B_y \sin B \cos L - B_x \sin L. \quad (7)$$

The right-handed coordinates x, y, and z are defined so that z is normal to the solar surface and y is tangent to the great circle passing through this point and the north pole. In Figure 17, we present plots of the longitudinal field as a function of azimuthal angle and tilt angle at representative points on the east half of the solar disk. Plots for the west half of the disk are mirror images in azimuth of the plots in Figure 17. Here, azimuthal angle is measured in degrees clockwise from north and tilt angle ranges from 0° (vertical) to 90° (horizontal). The E0N30 plot is different from the E30N0 plot by a 90°shift in azimuth, and the E0S30 plot by a 180° shift in azimuth.

At disk center, the longitudinal field is a strictly decreasing function of tilt angle. Therefore, any decrease in longitudinal field there can only be associated with an increase in tilt. In every other plot, the picture is more complicated. We discuss a simple example.

Suppose that the active region is a simple bipolar loop system with both polarities lying on $B = 0$ (middle row of plots in

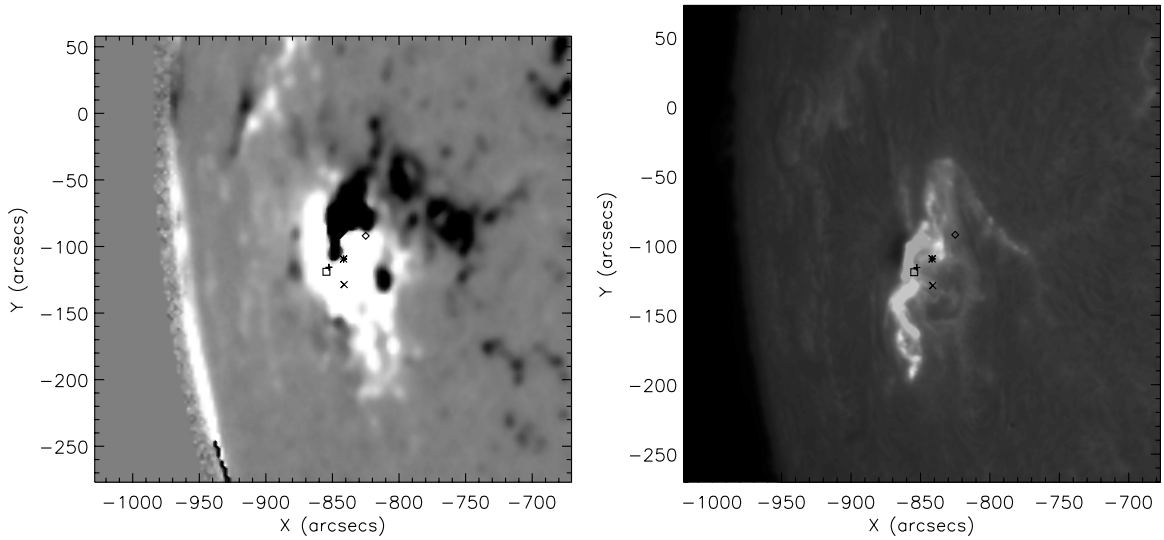

Figure 14. Left: a blow-up of the full-disk image of Figure 2 showing AR10930 and the centroids of selected flare signatures. The square (□) represents the centroids of *RHESSI* X-ray (6–12 keV and 100–300 keV) and ISOON white-light emission, from Balasubramaniam et al. (2010). The asterisk (*) marks the centroid of magnetic force changes between 18:30 and 18:40 UT. The plus (+) and cross (×) symbols the centroids of the two contiguous regions of force changes between 18:40 and 18:44 UT. The diamond (◇) marks the radiant point of the associated Moreton wave studied by Balasubramaniam et al. (2010). Right: ISOON Hα (red minus blue) image of the region at 18:43 UT with the same centroids marked.

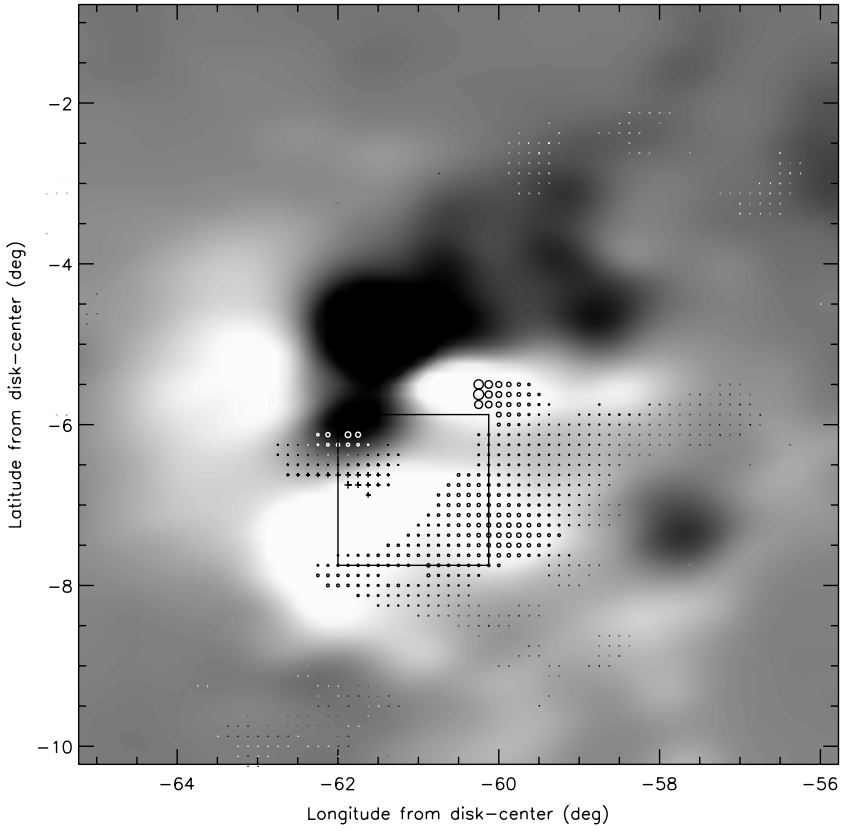

Figure 15. Spatial distribution of estimated force changes between 1830 UT and 1850 UT for the 2006 December 6 X6.5 flare. Plus signs (+) denote changes where the longitudinal field increased and circles (○) changes where the longitudinal field decreased. The symbol size represents the force change. The forces are overplotted on the remapped magnetogram of Figure 3. The black square represents the field of view of the mosaic plot in Figure 5.

Figure 17) and that the flux in the eastern polarity has an azimuth angle of −90° (the vector points to the west) and that the flux in the western polarity has an azimuth angle of +90° (the vector points to the east). Let us assume without loss of generality that the region is located in the eastern half of the solar disk. Then the eastern flux as a function of tilt angle has maximum value where the tilt angle matches the angular displacement $|L|$ from disk center. For example, if this eastern flux is at N0E30, N0E45, or N0E65, then its longitudinal component has maximum strength at tilt angle 30°, 45°, and 65°, respectively (see the longitudinal fields with −90° of azimuth in the middle row of plots in Figure 17). If, during a flare, the field becomes more horizontal (i.e., the tilt angle increases) according to Hudson et al. (2008) picture then the observed longitudinal

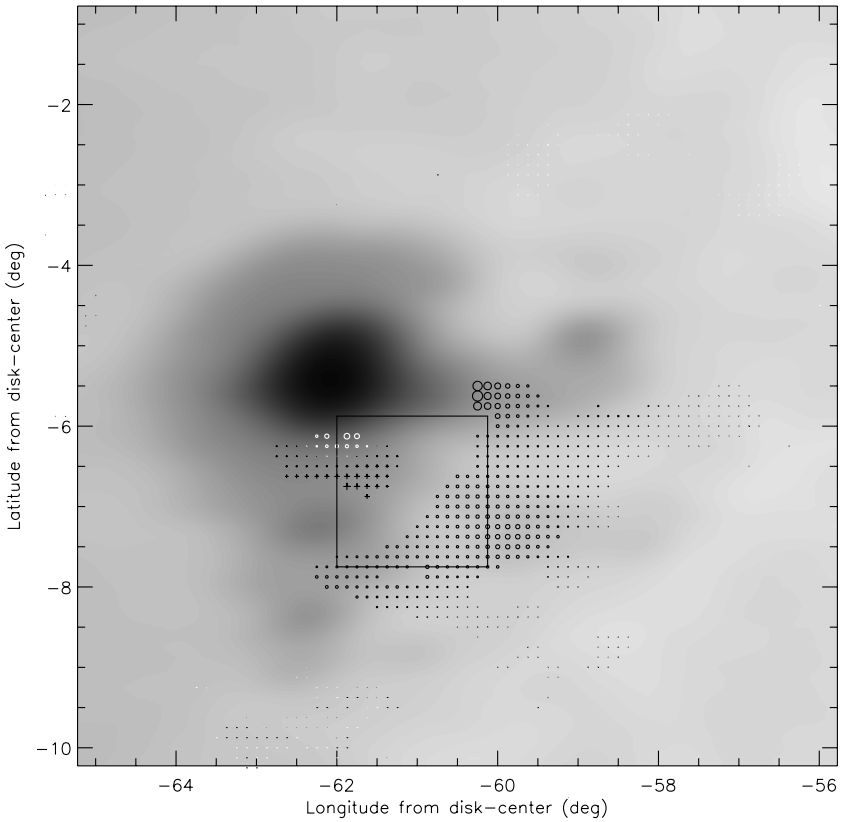

Figure 16. Spatial distribution of estimated force changes between 1830 UT and 1850 UT for the 2006 December 6 X6.5 flare overplotted on the remapped GONG continuum-intensity image. Plus signs (+) denote changes where the longitudinal field increased and circles (○) changes where the longitudinal field decreased. The symbol size represents the force change. The black square represents the field of view of the mosaic plot in Figure 5.

field in the eastern polarity would increase for tilt angles less than 30°, 45°, and 65° and would decrease for tilt angles greater than 30°, 45°, and 65°, respectively. On the other hand, if the azimuth angle is not exactly −90° then the longitudinal fields become more likely to decrease with increasing tilt. For flares at locations $B \neq 0$ (see the top and bottom rows of plots in Figure 17), the dependence of the longitudinal field on azimuth angle is offset. At all locations, even near the limb, longitudinal field decreases can accompany tilt increases if the tilt angle is large enough. As we have seen in Section 7 many of the fields that change most during flares are likely to be nearly horizontal (i.e., they are likely to have large tilt angle).

Now we consider the western polarity with eastward azimuth angle (+90°). If located on $B = 0$ (middle row of plots in Figure 17), the western longitudinal flux changes sign at a certain value of tilt. The negative values and white contours correspond to angles where the unit vector points away from the observer and its longitudinal component is negative. This can happen when the field vector has azimuth angle pointing away from disk center and the field is sufficiently tilted. For example, if the flux is at N0E30, N0E45, or N0E65 then its longitudinal component changes sign at tilt angle 60°, 45°, and 25°, respectively (see the longitudinal fields with +90° of azimuth in the middle row of plots in Figure 17). If, during a flare, the field becomes more tilted according to Hudson et al. (2008) picture then the observed longitudinal field strength in the western polarity would decrease for tilt angles less than 60°, 45°, and 25° and would increase for tilt angles greater than 60°, 45°, and 25°, respectively.

In general, the active regions in our data set are too complex for us to be able to characterize them in this way as bipolar loop systems with known azimuth and tilt angles. Our observations only include information on the longitudinal field component. We would need good vector observations to determine with confidence the azimuthal and tilt angles of any given field. Without such observations, however, we can describe where in the tilt-azimuth parameter space the longitudinal field is an increasing or decreasing function of tilt. Let us assume that the total field strength does not change significantly during the flare and that the longitudinal field change is caused only by an increase in tilt toward horizontal according to Hudson et al. (2008) picture. To see where in the parameter space the longitudinal field would increase or decrease under such conditions we explore in the plots trajectories of constant azimuth angle and increasing tilt, i.e., trajectories of decreasing y-coordinate in the plots, and note whether the fields increase or decrease in strength along these trajectories.

For example, in the disk-center plot (right plot in middle row of Figure 17), all longitudinal fields decrease in strength along such trajectories, as expected, whereas in the N0E65 plot (left plot in middle row of Figure 17) approximately half of the longitudinal fields increase and half decrease. Therefore, even 65° away from disk center, the longitudinal field is approximately equally likely to increase or decrease if the tilt angle increases. Within about 65° of disk center, the longitudinal field decreases in most of the parameter space because of the prevalent top heaviness of the contours, so the longitudinal field is more likely to decrease than increase if the tilt angle increases. The white contours and the contours located above locations where $B_l = +1$ represent the subset of the parameter space where the longitudinal field increases if the tilt angle

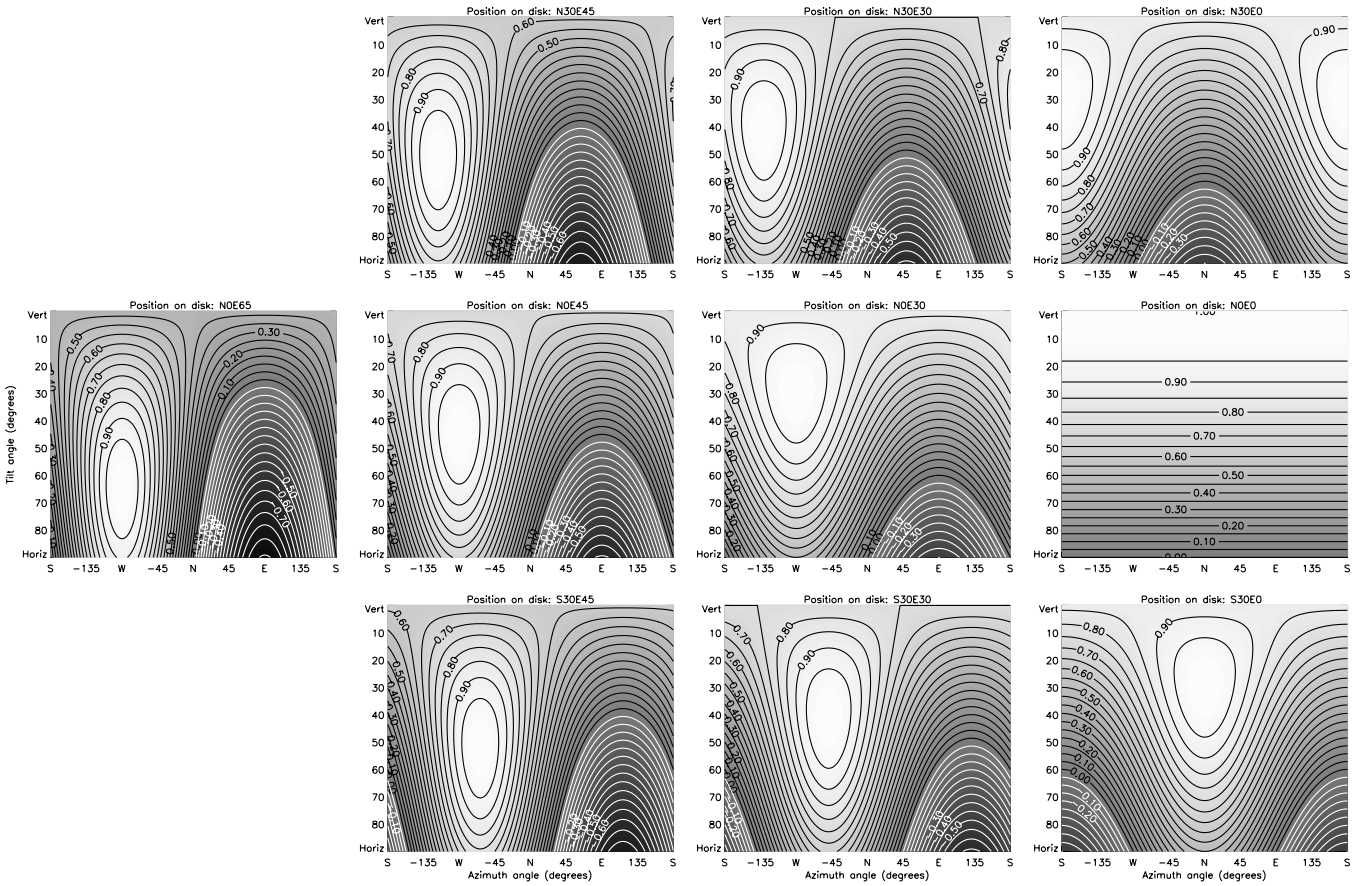

Figure 17. Contour maps of the longitudinal magnetic field component B_l of a unit vector as a function of the local tilt and azimuth angles. Maps corresponding to different positions on the east half of the solar disk, indicated by the titles, are shown. See the text for details.

increases. When a unit field vector pointing away from the observer increases in tilt at an azimuth angle pointing away from disk center, its longitudinal component increases in strength. Likewise when a unit vector off disk center has tilt angle less than its heliocentric angle then an increase in tilt toward disk center will result in an increase in longitudinal field strength. Under all other conditions an increase in tilt, i.e., a field vector becoming more horizontal, will result in a decrease in longitudinal field strength. Figure 17 shows that within about 65° of disk center the longitudinal field is more likely to decrease than increase if the tilt angle increases as predicted by Hudson et al. (2008), and that this bias should be greater near disk center than near the limb.

Is such a pattern to be found in our results? The statistics in Section 4 show that the observed longitudinal fields overall decreased more often than increased (94:65) and that this pattern is stronger in measurements near disk center (42:23) than near the limb (52:42). The pattern is more pronounced for weak (dB_l < 100 G) longitudinal field changes (71:37 all weak changes, 36:17 near disk-center, 35:20 near the limb) whereas the strong longitudinal field changes (dB_l > 100 G) do not show a statistically significant pattern. Unsigned longitudinal magnetic flux also tended to decrease during flares both near disk center and near the limb (Section 5). The unsigned longitudinal magnetic flux decreased during 3/4 of X-class flares near disk center compared to nearly 2/3 of X-class flares near the limb. The pattern described at the end of the previous paragraph is indeed evident in our results, giving observational support to Hudson et al. (2008) prediction that photospheric fields become more horizontal during flares.

10. CONCLUSION

It is now clear that the photospheric field does change during flares in general. Extending the pioneering work of SH05 to an enlarged data set of 77 M- and X-class flares, we have reported here various separate statistics for strong/weak longitudinal field changes, X-class/M-class flares and near-disk-center/near-limb events. As well as local longitudinal field intensity changes, we calculated changes in longitudinal magnetic fluxes. Whereas we selected only a few particularly clean pixels to represent field intensity changes of each flare, we used all pixels meeting quality-control criteria to calculate magnetic flux changes.

A summary of our results appears below.

1. The median of the absolute values of the most significant and abrupt, localized changes in the longitudinal magnetic field is larger for X-class flares than M-class flares (82 G compared to 54 G) and for limb flares than disk-center flares (85 G compared to 54 G).
2. Overall, local, longitudinal field changes are 1.4 times more often associated with a decrease in the background field than an increase. In more specific terms, weak-field changes, $|dB_l|$ < 100 G, are nearly twice as likely to decrease the field as increase it, and more than twice as likely near disk center, whereas strong-field changes, $|dB_l|$ > 100 G, are slightly more likely to increase the field.
3. Overall, we find no correlation between the field changes and the background field intensities, but we do find that weak-field changes, $|dB_l|$ < 100 G, show a modest

negative correlation with background intensity and that this correlation is stronger near disk center than near the limb.

4. Unsigned flux decreases for nearly two-thirds of the flares overall, for those near disk center and for those near the limb. For X-class flares, the ratio of decreases to increases is greater than 2:1. Unsigned flux tended to decrease during flares near disk center and near the limb. All six net flux changes of size 2×10^{20} Mx or greater decreased the net flux. The correlations between flux and flux changes were stronger near the limb than near disk center because the largest flux changes occurred in X-class flares near the limb.
5. The field change, the net flux change, and the net unsigned flux change, all show some modest correlation with *GOES* X-ray flux. The correlation between field change and *GOES* X-ray flux is dominated by X-class flares at the limb. We see a more significant correlation between net flux change and *GOES* X-ray flux at disk center than at the limb and a more significant correlation between unsigned flux change and *GOES* X-ray flux at the limb than at disk center. This may connect X-ray flux emission with asymmetric vertical flux changes.
6. We also found a clear preference for the large changes in magnetic field intensity, net magnetic flux and unsigned magnetic flux to occur near the limb. None of the large changes in these quantities occurred near disk center. Because the longitudinal fields change most near the limb and the line-of-sight direction is nearly horizontal near the limb, the data are consistent with the fields being nearly horizontal in the regions where we detect the largest field changes.
7. We estimated Lorentz force changes using A. N. McClymont's method. In seven X-class cases, we find force changes on the order of 10^{22} dynes, comparable to Hudson et al. (2008) estimate for a force change large enough to power a subsurface seismic wave. We also found evidence that force changes are associated more with decreases than increases in the longitudinal field, which is consistent with these forces being preferentially directed toward rather than away from the Sun. They are therefore consistent with Hudson et al.'s (2008) picture of photospheric fields becoming more tilted during flares and may be important in the generation of seismic waves.
8. By considering the possible relations between actual magnetic vector tilts and the associated longitudinal field components at chosen locations on the solar disk, we found that if the field tilt only increases (the vector becomes more horizontal) during a flare, the longitudinal field can either increase or decrease, whether near disk center or near the limb. However, decreases would likely outnumber increases at all parts of the disk that we investigated (within 65° of disk center) and more so near disk center than near the limb. We find such patterns in our data, again consistent with Hudson et al.'s (2008) picture of photospheric fields becoming more horizontal during flares.

While this work is based on a large data set, about 20,000 magnetograms, the physical picture that emerges is incomplete. Additional information could fill significant gaps in our understanding of the fields studied here. Since 2002 May/June 1 minute continuum-intensity images have been produced by the GONG network. Using these we can determine how strong-field changes and penumbral intensity changes are related. Umbral changes are more difficult to detect because umbral fields are very strong resulting in higher noise levels and because the dark umbral background makes flare-induced line profile transients more likely.

To investigate the relationship between the observed photospheric field changes and related changes in the corona, the magnetograms need to be supplemented with observations of higher atmospheric layers, such as Hα filaments and EUV loops. Using images from NASA's *Transition Region and Coronal Explorer* (*TRACE*) satellite, SH05 found excellent spatio-temporal agreement between changes in the photospheric magnetic field and increases in brightness at footpoints of flare ribbons. SH05 also found that the magnetic field changes appeared to cross the active regions at speeds ranging from 5 to 30 km s^{-1}. Using Hα images from Yunnan Observatory for one flare, they found a strong spatio-temporal correlation between a propagating magnetic field change and the motion of an Hα ribbon. Further simultaneous observations of propagating field changes and flare ribbon motions might shed much light on the causes of the field changes. Of the 15 flares that SH05 studied, they analyzed EUV data for three of them and Hα data for one. These were very laborious procedures because of the differing spatial and temporal resolutions, fields of view (and vantage point in the case of *TRACE*) and because the Hα and EUV signals derive from above the photosphere. However, this kind of work is essential if we are to understand the interactions between the photosphere and the corona.

This work has focused on the longitudinal field and flux changes without studying the changing morphology of the fields and their interactions during flares. A feature-tracking algorithm such as YAFTA[3] (Welsch & Longcope 2003) can identify magnetic flux systems and trace their evolution and interaction in time. Preliminary experiments with the magnetograms for the 2006 December 6 X6.5 flare show abrupt morphological changes corresponding to the stepwise field changes reported here. A future study will characterize this behavior.

Finally, the interpretation of these observations of longitudinal field changes is complicated by the fact that they do not include the full field vector. Sensitive, high-cadence vector data from the Vector Spectro-magnetograph (VSM) instrument on NSO's Synoptic Optical Long-term Investigation of the Sun (SOLIS) telescope and from the Helioseismic and Magnetic Imager (HMI) on board NASA's Solar Dynamics Observatory (SDO) spacecraft will allow us to extend this work in various ways. Kubo et al. (2007) studied a time series of *Hinode* vector data of AR10930 with 4 minute cadence covering the 2006 December 13 flare revealing many interesting field changes, but did not investigate abrupt stepwise changes in the vectors. We can verify using VSM or HMI that the longitudinal field changes are caused by changes in direction as we expect and not strength, determine whether the field vectors become more or less tilted with respect to the vertical during flares and derive estimates of full Lorentz force vectors associated with the field changes.

We thank the referee for comments that helped us to write a more readable manuscript. We thank Brian Harker, Jack Harvey, and Frank Hill for stimulating discussions and helpful comments on the manuscript and Sean McManus for reading very many images from tape. We also thank Pete Marenfeld for adding the color to Figure 5. This work utilizes data obtained by the Global Oscillation Network Group (GONG) program, managed by the National Solar Observatory, which is

[3] http://solarmuri.ssl.berkeley.edu/~welsch/public/software/YAFTA

operated by AURA, Inc. under a cooperative agreement with the National Science Foundation. The data were acquired by instruments operated by the Big Bear Solar Observatory, High Altitude Observatory, Learmonth Solar Observatory, Udaipur Solar Observatory, Instituto de Astrofísica de Canarias, and Cerro Tololo Interamerican Observatory.

REFERENCES

Anwar, B., Acton, L. W., Hudson, H. S., Makita, M., McClymont, A. N., & Tsuneta, S. 1993, Solar Phys., 147, 287
Aschwanden, M. J. 2004, Physics of the Corona, An Introduction (New York: Springer)
Balasubramaniam, K. S., et al. 2010, ApJ, 723, 587
Brockman, A. 2010, in ASP Conf. Ser., Proc. GONG 2008/SOHO XXI Workshop, Solar-stellar Dynamos as Revealed by Helio- and Asteroseismology, ed. M. Dikpati et al. (San Francisco, CA: ASP), 416
Deng, N., Liu, C., Yang, G., Wang, H., & Denker, C. 2005, ApJ, 623, 1195
Edelman, F., Hill, F., Howe, R., & Komm, R. 2004, in Proc. SOHO 14/GONG 2004 Workshop, Helio- and Asteroseismology: Towards a Golden Future, ed. D. Danesy (ESA SP-559; Noordwijk: ESA), 416
Fisher, G. H., Bercik, D. J., Welsch, B. T., & Hudson, H. S. 2010, arXiv:1006.5247v1
Fletcher, L., & Hudson, H. S. 2008, ApJ, 675, 1645
Gallagher, P. T., Moon, Y.-J., & Wang, H. 2002, Solar Phys., 209, 271
Hagyard, M. J. 1987, Solar Phys., 107, 239
Harvey, J. 1986, in Small-Scale Magnetic Flux Concentrations in the Solar Photosphere, ed. W. Deinzer, M. Knölker, & H. Voight (Göttingen: Vandenhoeck & Rupprecht), 25
Hudson, H. S. 2000, ApJ, 531, L75
Hudson, H. S., Fisher, G. H., & Welsch, B. T. 2008, in ASP Conf. Ser. 383, Subsurface and Atmospheric Influences in Solar Activity, ed. R. Howe et al. (San Francisco, CA: ASP), 221
Kosovichev, A. G., & Zharkova, V. V. 1999, Solar Phys., 190, 459
Kosovichev, A. G., & Zharkova, V. V. 2001, ApJ, 550, L105
Kubo, M., et al. 2007, PASJ, 59, 779
Leka, K. D., & Barnes, G. 2007, ApJ, 656, 1173
Li, Y., Jing, J., Tan, C., & Wang, H. 2009, Sci. China Ser. G, 52, 1702
Liu, C., Deng, N., Liu, Y., Falconer, D., Goode, P. R., Denker, C., & Wang, H. 2005, ApJ, 622, 722
Martínez-Oliveros, J. C., & Donea, A.-C. 2009, MNRAS, 395, L39
Mei, Z., & Lin, J. 2008, New Astron., 13, 526
Patterson, A. 1984, ApJ, 280, 884
Priest, E. R. 1982, Solar Magnetohydrodynamics (Dordrecht: Reidel)
Priest, E. R., & Forbes, T. G. 2000, Magnetic Reconnection (Cambridge: Cambridge Univ. Press)
Priest, E. R., & Forbes, T. G. 2002, A&AR, 10, 313
Qiu, J., & Gary, D. E. 2003, ApJ, 599, 615
Rust, D. M. 1974, in Flare-Related Magnetic Field Dynamics, ed. Y. Nagkagawa & D. M. Rust (Noulder: HAO/NCAR), 243
Sakurai, T., & Hiei, T. 1996, Adv. Space Res., 17, 91
Schrijver, C. J. 2007, ApJ, 655, 117
Spirock, T. J., Yurchyshyn, V. B., & Wang, H. 2002, ApJ, 572, 1072
Sudol, J. J., & Harvey, J. W. 2005, ApJ, 635, 647
Wang, H. 2006, ApJ, 649, 490
Wang, H., Ewell, M. W., Zirin, H., & Ai, G. 1994, ApJ, 424, 436
Wang, H., & Liu, C. 2010, ApJ, 716, L195
Wang, H., Liu, C., Deng, Y., & Zhang, H. 2005, ApJ, 627, 1031
Wang, H., Qiu, J., Jing, J., Spirock, T. J., & Yurchyshyn, V. 2004, ApJ, 605, 931
Wang, H., Spirock, T. J., Qiu, J., Ji, H., Yurchyshyn, V., Moon, Y.-J., Denker, C., & Goode, P. R. 2002, ApJ, 576, 497
Wang, H., Varsik, J., Zirin, H., Canfield, R. C., Leka, K. D., & Wang, J. 1992, Solar Phys., 142, 11
Wang, J., Zhao, M., & Zhou, G. 2009, ApJ, 690, 862
Welsch, B. T., Li, Y., Schuck, P. W., & Fisher, G. H. 2009, ApJ, 705, 821
Welsch, B. T., & Longcope, D. W. 2003, ApJ, 588, 620
Yurchyshyn, V. B., Wang, H., Abramenko, V., Spirock, T. J., & Krucker, S. 2004, ApJ, 605, 546
Zhang, H., Ai, G., Yan, X., Li, W., & Liu, Y. 1994, ApJ, 423, 828